# Mixing time prediction in stirred tanks using empirical methods and computational fluid dynamics

Gustav Bågmark


LUND UNIVERSITY

LTH
FACULTY OF ENGINEERING

Faculty of Engineering
Lund University
Sweden
2024-06-03

## Acknowledgement

I would like to express my sincere gratitude to my supervisor at Tetra Pak, Dragana, for her exceptional guidance and insightful discussions throughout the duration of this master's thesis. Her expertise in the field of CFD and mixing have been invaluable, and her support to help me through rough patches in the thesis has been much appreciated. I would also like to extend my heartfelt appreciation to my university supervisor Johan Revstedt for him always keeping a critical yet supportive eye on my work using his remarkable expertise in fluid mechanics, CFD and report writing. Furthermore, I would like to thank Emma Gustavsson and Joel Van Lunteren from FS Dynamics for being a huge help in learning and working with STAR CCM+, as well as for producing some of the ground work required for completing this thesis. Also, I am grateful to my colleagues at Tetra Pak who last year produced the experimental mixing time data used in this thesis, which has been very valuable.

Finally, thank you to my friends and family for supporting me throughout this thesis and my academic journey in general, it would not have been possible without you.

Lund, June 2024
Gustav Bågmark

This degree project for the degree of Master of Science in Biotechnology Engineering has been conducted at the Department of Process and Life Science Engineering, Faculty of Engineering, Lund University.

Supervisor at the Faculty of Engineering was Professor Johan Revstedt.

Supervisor at Tetra Pak Processing Systems was Dragana Arlov.

Examiner at Lund University was Docent Andreas Håkansson.

The project was conducted in collaboration with Tetra Pak Processing Systems AB.

Thesis for the Degree of Master of Science in Biotechnology Engineering

Department of Process and Life Science Engineering

Faculty of Engineering, Lund University

Box 118, 221 00 Lund

Sweden

**Abstract**

Stirred tanks are essential components in design and optimization of food processing lines, as they assure proper mixing and homogenization of ingredients. In this context, the mixing time is one of the most impactful performance parameters affecting various process design decisions. Thus, reliable methods to accurately predict mixing times in stirred tanks are highly desired.

The aim of this thesis is to expand Tetra Paks knowledge in mixing time prediction by using empirical methods and computational fluid dynamics (CFD) to predict the mixing time in one of their pilot tanks. Experimental mixing times had been produced prior the thesis, which are used to compare and validate the predictions against. CFD is used by developing a mixing time prediction method based on recent research that uses mean age theory (MAT).

CFD simulations of the pilot tank were conducted using two different agitators, one multi-impeller setup with baffles (MI setup) and one single-impeller setup without baffles (SI setup). The SM method was used in the simulations where various mean age distributions were extracted and used to obtain mixing time predictions, which were compared with the experimental data and empirical predictions.

For the MI setup, we found that an empirical method performs well in the turbulent and transitional regime. The CFD method also provides accurate predictions in the turbulent regime, and in the transitional regime with some method tweaks. This is however deemed less useful due to the accuracy of the less time consuming empirical method. Neither empirical methods nor CFD were able to predict the mixing time in the laminar regime. For the SI setup, we found that its dissatisfactory mixing performance makes the empirical predictions inadequate, and that the CFD method gave proper predictions with some method tweaks. Generally, we concluded that a CFD method is valuable in the laminar regime and for the SI setup where empirical correlations lack applicability and performance. However, the tweaks required using the MAT method makes it significantly less robust, why other CFD methods are considered more suitable in comparison to MAT in its current state.

**Keywords**— mixing time, mixing time prediction, mixing time correlations, CFD, mean age theory

# Nomenclature

## Symbols

| Symbol | Description | Units |
|---|---|---|
| $C$ | Passive scalar concentration | mole/m$^3$ |
| $D$ | Impeller diameter | m |
| $D_{eff}$ | Effective diffusivity | m$^2/s$ |
| $D_{k\omega}$ | k-omega model parameter | - |
| $D_{\omega}$ | k-omega model cross diffusion term | - |
| $E$ | Magelli correlation parameter | - |
| $E(a_s)$ | Scaled mean age PDF | - |
| $F$ | Force | N |
| $F_1$ | k-omega model parameter | - |
| $H$ | Tank liquid height | m |
| $J$ | Number of impellers, Magelli correlation | - |
| $K$ | Consistency index | Pa s$^n$ |
| $N$ | Impeller speed | Rotations per second |
| $N_P$ | Power number | - |
| $N_Q$ | Flow number | - |
| $P$ | Power | W |
| $Q$ | Impeller pumping capacity | m$^3/s$ |
| $R$ | Tank radius | m |
| $Re$ | Reynolds impeller number | - |
| $Sc$ | Schmidt number | - |
| $T$ | Tank diameter | m |
| $U_i$ | Velocity vector, i direction | m/s |
| $\overline{U_i}$ | Time averaged velocity, i direction | m/s |
| $V$ | Tank volume | m$^3$ |
| $a$ | Mean age | s |
| $a_s$ | Scaled mean age | - |
| $\overline{a_V}$ | Volume average mean age | s |
| $c$ | Helical ribbon wall clearance | m |
| $e$ | Impeller eccentricity | m |
| $h$ | Helical ribbon impeller height | m |
| $k$ | Turbulence kinetic energy | m$^2/s^2$ |
| $k_s$ | Metzner Otto parameter | - |
| $n$ | Behavior index | - |
| $n_b$ | Number of helical ribbon blades | - |
| $p$ | Helical ribbon impeller pitch | m per $360^0$ |
| $p$ | Pressure | Pa |
| $t$ | Time | s |
| $u_i^{'}$ | Turbulent velocity fluctutation, i direction | m/s |
| $v(a_s)$ | Cell volume | m$^3$ |
| $w$ | Helical ribbon impeller blade width | m |
| $x_i$ | Distance, i direction | m |

## Greek symbols

| Symbol | Description | Units |
|---|---|---|
| $\Lambda$ | Impeller torque | N m |
| $\alpha$ | Mean age scaling exponent | - |
| $\beta$ | mean age scaling exponent | - |
| $\beta_0$ | Mean age scaling exponent | - |
| $\dot{\gamma}$ | Shear rate | $s^{-1}$ |
| $\epsilon_p$ | Power dissipation rate | W/kg |
| $\zeta$ | Metzner Otto parameter | - |
| $\theta_C$ | Circulation time | s |
| $\theta_x$ | Mixing time, x% degree homogeneity | s |
| $\mu$ | Dynamic viscosity | Pa s |
| $\mu_a$ | Apparent dynamic viscosity | Pa |
| $\mu_t$ | Turbulent viscosity | Pa s |
| $\rho$ | Density | $kg/m^3$ |
| $\sigma_k$ | k-omega model parameter | - |
| $\sigma_\omega$ | k-omega model parameter | - |
| $\sigma_{\omega 2}$ | k-omega model parameter | - |
| $\sigma_{95}$ | Experimental 95 % mixing time standard deviation | s |
| $\tau$ | Shear stress | Pa |
| $\omega$ | Specific turbulence dissipation rate | 1/s |
| $\omega_0$ | k-omega model parameter | - |

## Abbreviations

| Abbreviation | Description |
|---|---|
| CFD | Computational fluid dynamics |
| MAT | Mean age theory |
| MI setup | Multi-impeller setup |
| MRF | Multiple reference frames |
| NZ | Non-zoning |
| PBT | Pitched blade turbine |
| PDF | Probability distribution function |
| RANS | Reynolds-averaged Navier-Stokes |
| RPS | Rotations per second |
| RT | Rushton turbine |
| SI setup | Single-impeller setup |
| SM | Sliding mesh |
| TS | Tip speed |
| WZ | With zoning |

# Contents

# List of Figures

# List of Tables

# 1 Introduction

## 1.1 Background

Every day, large amounts of food are processed and converted into various food products. With the objective of meeting consumers' nutritional needs, preferences, and safety standards, the industry employs a variety technologies for delivering food products. At the core of this lies processing equipment utilized in various unit operations, encompassing an extensive range of machinery designed to handle stages from raw material preparation to final packaging.

Essential components in this context are stirred tanks, the primary function of which is to ensure proper mixing and homogenization of ingredients. Other sub-duties of stirred tanks include enhancing heat transfer, enhancing mass transfer and providing a controlled environment for chemical reactions. Whether dealing with liquids, solids, or gases, the agitation facilitated by stirring mechanisms within the tank promotes the consistent distribution of ingredients. Tetra Pak Processing is a company manufacturing different processing equipment, such as homogenizers, heat exchangers, aspectic tanks and stirred tanks, but also designs and delivers food processing lines.

The efficacy of stirred tanks is crucial, as inadequate mixing performance can result in detrimental consequences for productivity, efficiency, and economy. In the U.S. chemical industry alone, an estimated loss ranging from 1 to 10 billion dollars in 1989 was attributed to inefficient mixing [9]. The pharmaceutical industry is another example where there are yearly costs in the order of 500 million dollars due to bad mixing performance in scale-up and process development [10]. One aspect of the mixing performance is the mixing time, defined as the time required to reach a certain degree of homogeneity in the tank. The mixing time can be determined experimentally, or predicted using various methods. A satisfactory ability to predict the mixing times in stirred tanks aids when making decisions on what tank design and agitator are most suitable for a certain process, and is generally highly desired in scale up and mixing performance optimization.

There exists a wide variety of methods for prediction of the mixing time. Some of these involve the use of empirical correlations developed at several different institutions in the last century. In recent decades however, the use of methods based on computational fluid dynamics (CFD) has seen a significant increase. CFD is based on numerical solutions of the partial Navier-Stokes equations governing fluid flow, enabling simulation of the fluid flow in e.g. stirred tanks. These methods can be highly effective since a properly developed and validated CFD methodology can significantly reduce the need for experiments, which can be more expensive. Use of CFD also enables one to be pro-active in important decision making, such as which agitator setup to use in different scales for a specific food product. Recently, a new mixing time prediction method based on mean age theory (MAT) has also emerged as an option for CFD simulations [9, 8]. Naturally, to make confident predictions using both empirical and CFD methods, they need to be compared against experimental mixing time data. Combining empirical mixing time correlations, CFD methods and experimental data is thus of significant interest in mixing time prediction analysis.

## 1.2 Aim

This thesis aims to expand Tetra Paks knowledge and skills in making accurate mixing time predictions in stirred tanks they deploy in the food industry. The mixing time predictions will be done on one of Tetra Pak's pilot tanks with a volume of 200 L. Existing empirical mixing time correlations will be used and their mixing time prediction ability will be analyzed. Furthermore, a CFD method based on mean age theory will be developed and validated. Previous work at Tetra Pak has produced experimental mixing times which the mixing time predictions will be compared and validated against. The experiments were conducted using different agitators and liquids with varying viscosity and rheological behaviour. Solely miscible liquids were used in the experiments, meaning the aim of this thesis covers only miscible liquid mixing.

Both the empirical methods and the CFD method will be used and analyzed in terms of their mixing time prediction ability as well as their practicality and efficiency for the specific setups tested in this thesis. The overall goal is that this thesis will aid Tetra Pak when developing, scaling up and deploying their stirred tanks in various food processes.

## 1.3 Objectives

1. Expand knowledge on how empirical correlation methods can be used for prediction of mixing times in Tetra Pak's stirred tanks.
2. Develop a validated CFD methodology based on mean age theory for prediction of mixing times.
3. Evaluate the CFD methodology based on mean age theory in terms of its mixing time prediction ability and practicality.

# 2 Theory

## 2.1 Mixing

Mixing is generally defined as a process in which the degree of homogeneity of a mixture is increased. Based on the states of the compounds being mixed, mixing processes can be divided into different categories. These are miscible liquid mixing, solid-liquid mixing, gas-liquid mixing and immiscible liquid-liquid mixing [10]. Mixing in food processes can belong to different categories, e.g. depending on if the food product has solids or not. This thesis will focus on miscible liquid mixing.

Regardless of mixing category, stirred tanks are the most commonly used equipment for mixing processes.

### 2.1.1 Stirred tanks

Stirred tanks are designed to excel in mixing and homogenization processes. These vessels play a crucial role in ensuring the uniform distribution of ingredients, a critical factor in achieving consistent product quality in the food manufacturing sector. Stirred tanks employ various agitation mechanisms, such as impellers, propellers, or paddles, to induce fluid movement within the vessel. Like other unit operations, stirred tanks can be operated as a continuous, batch or fed-batch process.

A typical stirred tank is seen in Figure 1, with a centric agitator and a liquid height to vessel diameter ratio approximately equal to 1. $D$ [m] is the impeller diameter, $T$ [m] is the tank diameter, and $H$ [m] is the liquid height.

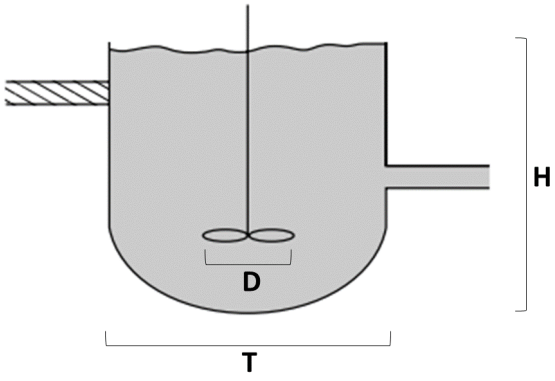


Figure 1: Stirred tank schematic [1]. Reprinted by permission.

### 2.1.2 Agitators and baffles

Two of the most frequently used impellers in stirred tanks are axial and radial impellers [2], images of which are shown in Figure 2. Axial impellers are designed to move fluid parallel to the axis of rotation, see Figure 3(a). As seen in the figure, the axial impeller pump axially downwards to the bottom of the tank. The fluid then moves up along the walls and then diverges inwards toward the impeller once again, completing the loop in a circulatory mixing pattern. Radial impellers on the other hand are designed to move fluid radially outwards from the center of rotation, see Figure 3(b). The figure illustrates how fluid is pumped radially towards the wall, where the fluid splits up and moves to both the top and bottom of the tank before diverging inwards and back to the radial impeller. Mixed flow impellers are impellers that are neither axial nor radial, where the Viscojet (Figure 2(c)) is an example of such an impeller. [11]. All three presented impeller types are turbine impellers.

The tank schematics in Figure 3 also depict vertical baffles attached to the walls. The purpose of including baffles is to improve mixing performance as an effect of the change in flow pattern. In Figure 3(d) the effect of including wall baffles is displayed viewed for the top of a tank with four baffles. Without the wall baffles (Figure 3(c)), the flow simply rotates in two dimensions and lack the top to bottom flow required for good mixing [2]. The baffles transform a purely tangential flow to a vertical flow, resulting in a more easily obtained

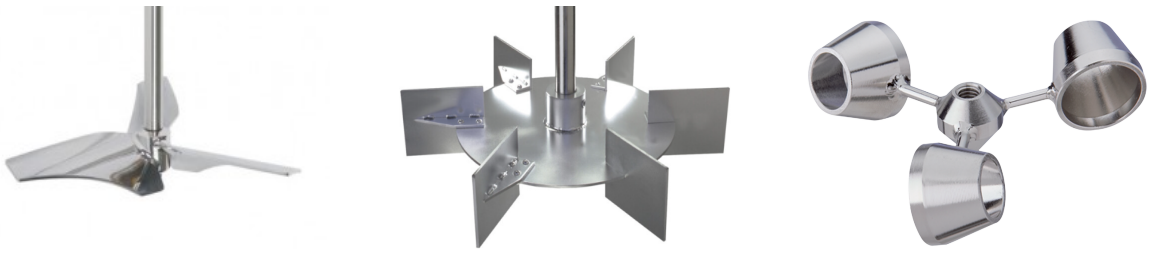

(a) (b) (c)

Figure 2: (a) Axial impeller (b) Radial impeller (c) Viscojet impeller

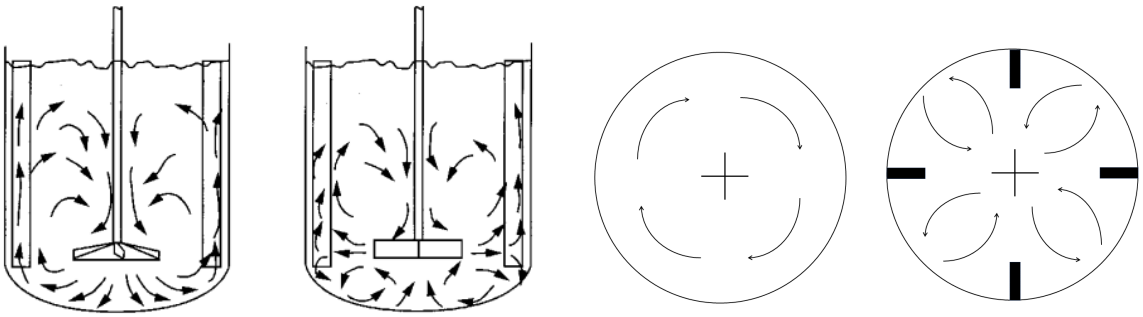

(a) (b) (c) (d)

Figure 3: (a) Axial impeller flow pattern (b) Radial impeller flow pattern [2], reprinted by permission (c) Flow pattern w/o baffles, top view (d) Flow pattern with baffles, top view

bottom to top mixing as observed in Figure 14(a) and (b). However, in tank and process setups that require regular cleaning, the use of baffles may be impractical [2].

### 2.1.3 Mixing flow regimes

Mixing processes can be characterized into different flow regimes, i.e. the laminar, turbulent and transitional flow regimes [12]. In laminar flow, viscous forces dominate, generally resulting in a non chaotic layered flow. Turbulent flow on the other hand occurs when inertial forces dominate the negligible viscous forces, and is characterized by the chaotic spread and interaction of small and large eddies in all directions. Dispersion of the fluid is thus rapid in the turbulent regime, causing significantly faster and improved mixing. The transitional region is the regime in between the laminar and turbulent flow regimes, in which both viscous and inertial forces are meaningful [12].

The flow regimes are often defined and analyzed with regards to the Reynolds number, which is a dimensionless number defined as the ratio between inertial and viscous forces. A geometrical factor is also included in the Reynolds number to account for the geometrical impact of the inertial forces. There exists a range of different Reynolds numbers depending on what the fluid process is. In the case for tank mixing processes, the Reynolds number is defined as in Equation 1.

$$Re = \frac{\rho N D^2}{\mu} \tag{1}$$

Where $\rho$ [kg/m$^3$] is the fluid density, $N$ [rps] is the impeller rotational speed, and $\mu$ [Pa s] is the fluid's dynamic viscosity. For tank mixing processes, the flow is generally considered laminar at Re $< 10$, fully turbulent at Re $> 10000$, and transitional in between [7]. A parameter which is often analyzed in connection to the different flow regimes and the Reynolds number is the dimensionless mixing time (see upcoming subsections for further descriptions of the mixing time). The dimensionless mixing time has generally been shown to be constant in the turbulent and laminar regime, while declining with increasing Re in the transitional regime [3]. See Figure 4 where the behavior in the different flow regimes is clearly observed.

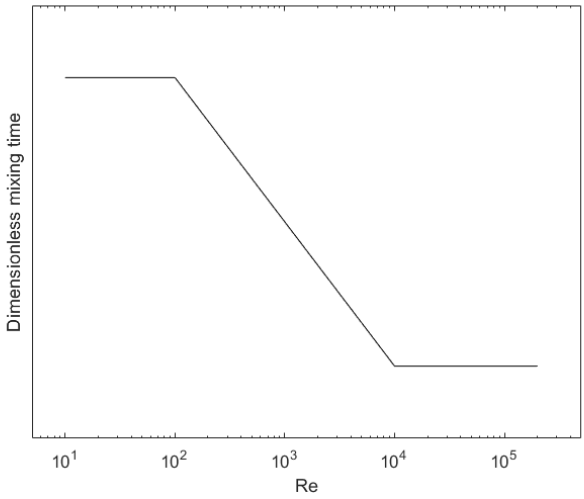


Figure 4: General trend of the dimensionless mixing time as a function of the Reynolds number [3].

### 2.1.4 Impeller parameters

The power number $N_p$ is a dimensionless number that provides information on the power requirements of an impeller and is defined as in Equation 2.

$$N_p = \frac{P}{\rho N^3 D^5} \tag{2}$$

Where $P$ [W] is the power requirement of the impeller. In the literature, there exists power number data for various impellers at different Reynolds numbers [7]. Graphs showing power numbers for different impellers as a function of the Reynolds number are depicted in Figure 5 [4]. The trend shows that the power number decreases in the laminar and transitional regime and converges to a constant value in the turbulent regime. One way of obtaining the power number of an impeller is by using this data from literature. It can also be determined experimentally by measuring the power requirement of the impeller, or through CFD simulations which is described in more detail later.

Another important impeller parameter is the flow number which is related to the impeller's ability to discharge the mixed fluid. It is defined as in Equation 3 [7].

$$N_Q = \frac{Q}{ND^3} \tag{3}$$

Where $Q$ [$m^3$/s] is the impeller pumping capacity which can determined experimentally for example through laser measuring techniques. It can also be calculated using CFD, where a surface needs to created in the discharge region of the impeller [7] in the CFD software. For an axial impeller pumping downwards, the surface is a circle below the axial impeller, and for a radial impeller, the surface is a cylinder around the impeller. The velocity is then to be integrated over these surfaces for determination of the impeller pumping capacity [7].

The circulation time $\theta_C$ [s], i.e. the time required for the fluid to circulate the tank once, is another variable that is also connected to the pumping capacity. It is often simply approximated using Equation 4 [13], where $V$ [$m^3$] is the tank liquid volume.

$$\theta_C = \frac{V}{Q} \tag{4}$$

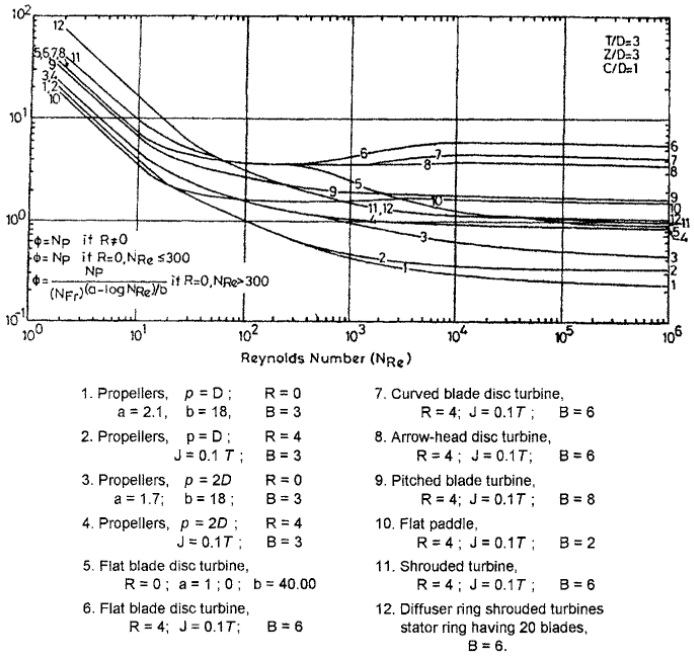


Figure 5: Power number for different impellers as a function of the Reynolds number [4]. Reprinted by permission.

### 2.1.5 Viscosity

The viscosity $\mu$ is a measure of a fluid's resistance to deformation and has a major impact on mixing processes and which flow regime the mixing occurs in. It is defined using the terms shear stress and shear rate which can be understood through the scenario depicted in Figure 6, where two red plates are incapsulating theoretical layers of a blue liquid. The bottom plate is stationary while the top plate starts to move at a constant velocity $v$, resulting in the liquid being deformed [14].

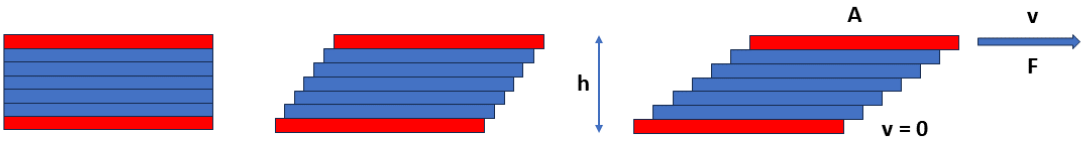


Figure 6: Depiction of fluid deformation.

The shear rate $\dot{\gamma}$ [$s^{-1}$] is a measure of a fluid's rate of deformation and is defined as in Equation 5.

$$\dot{\gamma} = \frac{v}{h} \tag{5}$$

Where $v$ [m/s] is the velocity and $h$ [m] is the distance between the theoretical plates in Figure 6. The shear stress $\tau$ [Pa] on the other hand is the stress causing the fluid deformation, and can be defined as in Equation 6.

$$\tau = \frac{F}{A} \tag{6}$$

Where $F$ [kg m/s$^2$] is the force acting on the top plate and $A$ [m$^2$] is the top area of the top plate. If a high shear stress is required to achieve a certain rate of deformation, then the fluid's resistance to deformation must be high as well and thus have a high viscosity. For a so called Newtonian fluid, the relationship between the shear stress and the shear rate is linear where the viscosity $\mu$ is the proportionality factor, as defined in Equation 7.

$$\tau = \mu\dot{\gamma} \tag{7}$$

Through the Newtonian relationship we again understand that a fluid with high viscosity requires a large shear stress for a certain rate of deformation, whereas a fluid with low viscosity requires a smaller shear stress for the same deformation rate. The viscosity for Newtonian fluids is constant, but that is not the case for non-Newtonian fluids. For non-Newtonian fluids, the relationship between the shear stress and the shear rate is nonlinear, meaning the viscosity is not a constant [15]. The relationship between the shear stress and the shear rate for a Newtonian and two non-Newtonian fluids are depicted in Figure 7(a).

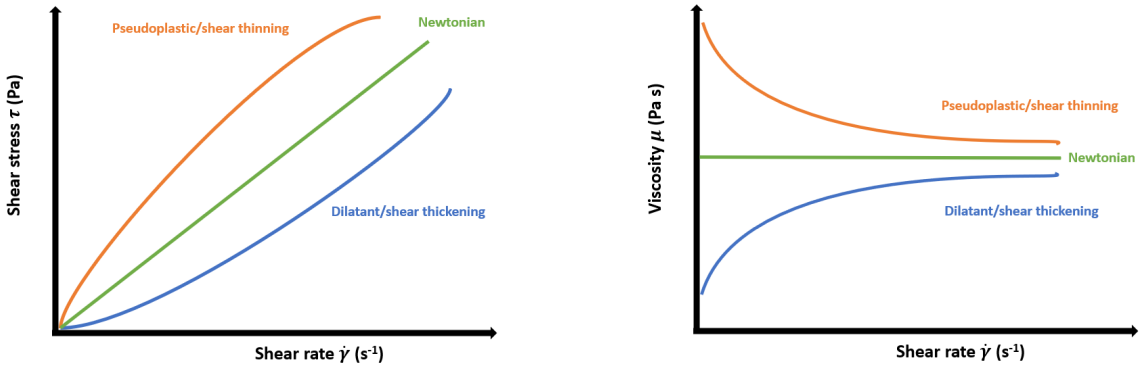


(a) (b)

Figure 7: (a) Shear stress vs shear rate for a Newtonian and two non-Newtonian fluids (Pseudoplastic and Dilatant) (b) Viscosity vs shear rate for a Newtonian and two non-Newtonian fluids

As is seen in Figure 7(a), the shear stress increases nonlinearly for the non-Newtonian pseudoplastic and dilatant fluids, entailing that their viscosities, also known as apparent viscosites, are varying. Dilatant fluids are shear thickening which results in higher apparent viscosity with increasing shear rate, and Pseudoplastic fluids are shear thinning, meaning the apparent viscosity decreases with increased shear rate. These behaviors are illustrated in Figure 7(b). Many liquid food products are shear thinning [16], and thus only shear thinning behavior will be dealt with in this thesis. The nonlinear relationship between the shear stress and shear rate for non-Newtonian fluids is often mathematically presented with a power law, see Equation 8 [16].

$$\tau = K\dot{\gamma}^n \tag{8}$$

Where $K$ [Pa s$^n$] is called the consistency index and $n$ is called the flow behavior index [16]. When n $< 1$ then we have a shear-thinning fluid, when n $> 1$ then we have a shear-thickening fluid and when n $= 1$ then we have a Newtonian fluid. The apparent viscosity of a non-Newtonian fluid can be expressed as in Equation 9, which is a combination of Equation 7 and 8.

$$\mu_a = K\dot{\gamma}^{n-1} \tag{9}$$

Since the viscosity of non-Newtonian fluids varies with the shear rate, there is often a need to approximate the shear rate in a stirred tank and then an apparent viscosity can be calculated. This is useful in scale up and design of manufacturing processes. A common approach is to approximate the shear rate using the method developed by Metzner and Otto [17], who concluded that the shear rate at the impeller is related to the impeller rotation speed in the laminar regime in accordance with Equation 10 [15].

$$\dot{\gamma} = k_s N^{\zeta} \tag{10}$$

Where $k_s$ and $\zeta$ are model parameters. $k_s$ assumes a value between 10 and 15 for turbine impellers such as axial and radial impellers, and $\zeta = 1$ in the laminar regime. Other authors have also analyzed the Metzner Otto method and determined that $\zeta = 1.5$ in the transitional regime, while still being equal to 1 in the laminar regime as Metzner and Otto suggested [15]. Using the Metzner Otto equation, the apparent viscosity at the impeller can be approximated for non-Newtonian fluids [15] using Equation 9.

## 2.2 Mixing time

Mixing performance can be evaluated in different ways, depending on what is considered most important for a certain mixing process. One mixing performance parameter is the mixing time, which will be the sole focus of this thesis. The mixing time is defined as the time required to achieve a certain degree of homogeneity in a stirred tank [15]. The desired degree of homogeneity varies depending on the context, but common degrees are 90%, 95% and 99%. A lot of previous work in the literature that is valuable for this thesis have been conducted using a 95% degree of homogeneity, and a 95% degree will be used in this thesis as well. Mixing time serves as one of the most important factors in liquid-liquid mixing and scale-up of mixing processes [13], as discussed in section 1.1.

The next subsection provides a brief description of the experimental method used for determining the mixing time, while subsequent subsections introduce the empirical and CFD methods that will be used for mixing time prediction.

## 2.3 Experimental mixing time

A wide range of experimental methods have been reported in the literature for determination of mixing times, where the decolorization method is a common one in terms of practicality [18]. Decolorization works by having a colored liquid continuously stirred in the tank, and subsequently adding a decolorization agent that reacts chemically with the colored liquid and forms a colorless compound. A 95% mixing time, $\theta_{95}$ [s], is then determined when 95% of the tank liquid is decolorized. Advantages of colorimetry include it being non-intrusive, direct, simple to implement and requiring no calibration [18]. The method also enables identification of zones with varying mixing performance within the tank, for example identification of dead zones with poor mixing [18]. Disadvantages include subjectivity of human perception and being usable only on transparent tanks and liquids.

## 2.4 Empirical mixing time correlations

This subsection aims to provide a thorough introduction to the empirical mixing time correlations used for mixing time prediction in this thesis. These correlations are generally based on different parameters, such as the impeller power number or the circulation time. As described previously, the development of the correlations have generally concluded that the dimensionless mixing time, i.e. the product of the mixing time and the impeller speed, is constant in the laminar and turbulent regime and decreasing in the transitional regime when plotted on a log-log scale against the Reynolds number [3], as displayed in Figure 4. Since the dimensionless mixing time has varied dependence on the Reynolds number, different mixing time correlations have been developed separately in the separate flow regimes. Firstly the correlations developed in the turbulent flow regime are presented.

### 2.4.1 Empirical mixing time correlations in the turbulent regime

The most commonly used mixing time correlations were developed by Grenville and will henceforth be referred to as the Grenville correlations [19].

#### Grenville turbulence correlation

The mixing time correlations based on the power number produced by Grenville [19] were developed using a baffled tank with an aspect ratio, i.e. the liquid height to tank diameter ratio, equal to 1. They used a single impeller system and varied the type of impeller (pitched blade, flat blade and hydrofoil turbines) and its

diameter [15] when developing the correlation. Grenville correlated the 95% mixing time data with the power number in both the turbulent and transitional regime, and obtained the turbulence correlation presented in Equation 11. The equation shows, as discussed previously, that the dimensionless mixing time only depends on geometry and the power number in the turbulent regime.

$$N\theta_{95} = 5.2\frac{T^{1.5}H^{0.5}}{D^2N_p^{1/3}} \tag{11}$$

The Grenville correlations are the most commonly used mixing time correlations based on the power number [15], but other authors have also developed mixing time correlations for other geometries.

### Cooke turbulence correlation

Cooke et al. developed a turbulence correlation using a range of multi impeller systems with an aspect ratio greater than 1. The correlation was based on using multiple radial Rushton impellers and is presented in Equation 12 [15], and will further on be referred to as the Cooke correlation.

$$N\theta_{95} = \frac{3.3}{N_p^{1/3}N}\left(\frac{H}{D}\right)^{2.43} \tag{12}$$

They found that the mixing time increased in these setups when compared to the Grenville correlation, the cause of which has since been attributed to zoning effects when using multiple radial impellers [20]. Zoning effects in a mixing process are the appearance of compartmentalized mixing zones with limited mixing between them, see Figure 8.

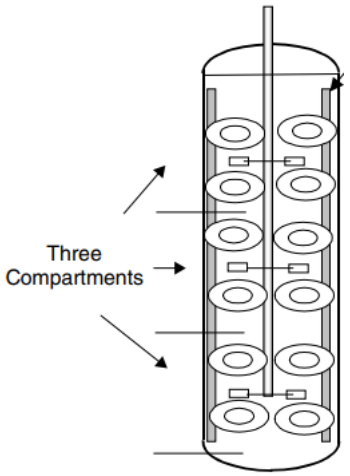


Figure 8: Compartmentalization in a stirred tank with multiple impellers [5]. Reprinted by permission.

### Magelli turbulence correlation

Magelli [20] also developed two mixing time correlations for tall multi impeller systems with aspect ratios larger than 1. The correlations were developed using impellers with sufficient space between them to be non-interacting. The correlations include the parameter $E$ defined as in Equation 13).

$$E = \frac{N_Q^3}{N_p}\left(\frac{D}{T}\right)^4 \tag{13}$$

The first correlation was developed using axial and mixed flow impellers and is presented in Equation 14. Magelli also studied systems with multiple radial impellers and found that the first correlation performed well when the radial impellers were positioned close enough for no zoning effects to appear, but overpredicted mixing times when the radial impellers were further apart which led to compartmentalized mixing zones [20].

Magelli thus modified the correlation to be usable in radial impeller setups with mixing zones, resulting in the second Magelli correlation presented in Equation 15.

$$\theta_{95} = 2.4(E\epsilon_p)^{-1/3} H^{2/3} J^{1/3} \tag{14}$$

$$\theta_{95} = 1.2(E\epsilon_p)^{-1/3} H^{2/3} \frac{J-1}{J^{\frac{2}{3}}} \tag{15}$$

Where $\epsilon_p$ [W/kg] is the power dissipation rate (power input over total liquid mass) and $J$ is the number of impellers. These correlations will henceforth be referred to as the no zoning (NZ) Magelli correlation (Equation 14) and the with zoning (WZ) Magelli correlation (Equation 15).

### Karcz turbulence correlation

Some tank setups do not include baffles and may have impellers that are eccentrical, i.e. not placed in the tank center. Karcz [21] developed a mixing time correlation in the turbulent regime for unbaffled tanks with varying impeller eccentricity. The correlation is presented in Equation 16.

$$\theta_{95} = 48.5 + \frac{1}{\Lambda} e^{\left[-1.89 \frac{1}{\Lambda}\left(\frac{e}{R}\right)\right]} e^{[8.18\Lambda]} \tag{16}$$

Where $\Lambda$ [N m] is the impeller torque, $e$ [m] is the impeller shaft's distance from the tank center, and $R$ [m] is the tank radius.

### Circulation time turbulence correlation

The circulation time correlation is based on correlating the circulation time with the mixing time, i.e. determining how many tank circulation are needed for complete mixing to be achieved. Sano [22] tested different impeller geometries in the turbulent regime and saw that the amount of circulations needed varied from three to four. Doran [23] also wrote that the correlation coefficient is approximately four, meaning the mixing time in the turbulent regime can be approximated using Equation 17.

$$\theta_{95} = 4\theta_C \tag{17}$$

### 2.4.2 Empirical mixing time correlations in the transitional regime

Grenville also correlated data in the transitional regime, resulting in the correlation presented in Equation 18. As discussed previously, the dimensionless mixing time decreases with increasing Reynolds number in the transitional regime, why the Reynolds number is included in the correlation.

$$N\theta_{95} = \frac{183^2}{N_p^{2/3} Re} \left(\frac{T}{D}\right)^2 \tag{18}$$

Grenville analyzed both Newtonian and shear thinning (non-Newtonian) fluids when developing these correlations [19]. Applying these mixing time correlations for shear thinning fluids is more complicated since they have varying viscosity depending on the local shear rate in the tank. In the turbulent regime however, there is no dependence on viscosity and thus no modification is needed. In the transitional regime, there is a dependence on the viscosity. One viable approach is to approximate the apparent viscosity at the impeller using the Metzner Otto method described in subsection 2.1.5. However, the approach that Grenville took was to determine the apparent viscosity at the wall, and use that viscosity to calculate the Reynolds number at the wall [19], and then use this Reynolds number in the transitional regime correlation. To determine the viscosity at the wall, the shear rate at the wall is needed. Grenville did this by first approximating the shear stress $\tau_W$ at the wall using Equation 19.

$$\tau_W = \frac{1}{1.622} \left(\frac{\Lambda}{T^3}\right) \tag{19}$$

The approximated shear rate $\dot{\gamma}_W$ at the wall was then calculated using Equation 20, followed by calculation of the viscosity $\mu_W$ at the wall using Equation 21 and Reynolds number $Re_W$ at the wall with Equation 22 [19].

$$\dot{\gamma}_W = \left(\frac{\tau_W}{K}\right)^{1/n} \tag{20}$$

$$\mu_W = K\dot{\gamma}_W^{n-1} \tag{21}$$

$$Re_W = \frac{\rho N D^2}{\mu_W} \tag{22}$$

With the approximation of the Reynolds number at the wall, the mixing time correlation in the transitional region can be used for shear thinning fluids.

### 2.4.3 Empirical mixing time correlations in the laminar regime

For mixing in the laminar regime, one of the most common impeller types to use is a helical ribbon impeller, see Figure 9.

Figure 9: Helical ribbon impeller [6]. Reprinted by permission.

Grenville thus developed a mixing time correlation in the laminar regime for helical ribbon impellers. The mixing time includes a geometrical factor $K_P$ which is presented in Equation 23, and the correlation is presented in Equation 24.

$$K_P = 82.8\frac{h}{D}\left(\frac{c}{D}\right)^{-0.38}\left(\frac{p}{D}\right)^{-0.35}\left(\frac{w}{D}\right)^{0.2} n_b^{0.78} \tag{23}$$

$$N\theta = 896 \times 10^3 \times K_P^{-1.69} \tag{24}$$

Where $h$ [m] is the impeller height, $c$ [m] is the wall clearance, $p$ is the impeller pitch, $w$ [m] is the impeller blade width and $n_b$ is the number of blades. Note that the degree of mixing homogeneity is not written as this was not specified by Grenville [19].

## 2.5 Computational fluid dynamics

A general introduction to CFD and its application for stirred tanks is provided in this subsection, followed by a description of how CFD will be used for mixing time prediction in the subsequent subsection.

Computational fluid dynamics is the numerical simulation of fluid motion, meaning mixing processes can be simulated and analyzed through the use of CFD. The simulation is based on numerical solution of the physical equations governing fluid flow.

### 2.5.1 Governing equations

The governing equations for fluid motion are derived based on several physical laws and conservation principles [7]. The first principle is conservation of mass, which states that the mass entering a fluid element must equal the mass leaving the fluid element. Using the conservation of mass principle, one can derive one of the governing equations known as the continuity equation. Often in CFD applications, the fluid density is assumed to be incompressible and thus have a constant density. With this assumption we arrive at the simplified form of the continuity equation presented in Equation 25 [7].

$$\frac{\partial U_i}{\partial x_i} = 0 \tag{25}$$

Where $U$ [m/s] is velocity and $x$ [m] is distance. The momentum equations are three additional governing equations expressing the conservation of momentum in all three directions in a fluid element. The equations can be derived using Newton's second law of motion and are known as the Navier-Stokes equations (NS), the generalized form of which are presented in Equation 26.

$$\frac{\partial(\rho U_i)}{\partial t} + \frac{\partial}{\partial x_j}(\rho U_i U_j) = -\frac{\partial p}{\partial x_i} + \frac{\partial}{\partial x_j}\left[\mu\left(\frac{\partial U_i}{\partial x_j} + \frac{\partial U_j}{\partial x_i}\right)\right] \tag{26}$$

Where $p$ [Pa] is the pressure. The presented equations comprise a system of partial differential equations that can be solved numerically in a mesh of discretized cells, meaning values of all flow variables, e.g. velocity and pressure, are solved and stored in every cell of the mesh. The most commonly used numerical method for solving the equations is the finite volume method [7].

CFD simulations can either be steady state simulations or transient ones. In steady state simulations, a certain fluid motion is solved in the state where it is no longer affected by time, meaning the flow field is time-independent. Transient simulations on the other hand aims to simulate how the fluid motion acts over time when starting from an initial state, i.e. time-dependent simulations.

Solving the governing equations can in principle be used for simulation of any fluid motion, including fully turbulent ones. However, due to the complexity and small scales of turbulence, resolving turbulent flows is extremely expensive in terms of computational resources, and is in most practical CFD applications not feasible. Still, most fluid motions in the world have turbulent characteristics, including mixing processes. Generally, there are three different approaches when handling turbulent simulations. The first is direct numerical simulation (DNS) which encompasses complete solution of the governing equations, meaning no modification of the equations are made. Using DNS is very computationally expensive and time consuming since all space and time scales are resolved. The other two approaches are large eddy simulation (LES) and the Reynolds-averaged Navier-Stokes (RANS) equation, both of which models the turbulence to make its simulation more feasible [7]. LES models the smaller turbulent scales while still resolving the larger turbulent eddies. RANS on the other hand models all turbulent scales and is thus the fastest and least computationally expensive, why it is the only one used in this thesis.

### 2.5.2 RANS Equations

The RANS equations are based on decomposing all transported variables, e.g. velocity, into a sum of a time averaged component and a fluctuating component. See Equation 27 for decomposition of the velocity $U_i$.

$$U_i = \overline{U_i} + u_i' \tag{27}$$

Where $U_i$ [m/s] is the time averaged velocity and $u_i$ [m/s] is the fluctuating component of the velocity. Substituting the decomposed variables into the continuity equation and the NS-equations and simplifying results in the RANS equations presented in Equation 28 and 29.

$$\frac{\partial \overline{U_i}}{\partial x_i} = 0 \tag{28}$$

$$\frac{\partial(\rho\overline{U_i})}{\partial t} + \frac{\partial}{\partial x_j}(\rho\overline{U_i}\,\overline{U_j}) = -\frac{\partial \overline{p}}{\partial x_i} + \frac{\partial}{\partial x_j}\left[\mu\left(\frac{\partial \overline{U_i}}{\partial x_j} + \frac{\partial \overline{U_j}}{\partial x_i}\right)\right] + \frac{\partial}{\partial x_j}(-\rho\overline{u_i' u_j'}) \tag{29}$$

Equation 29 is similar to the original momentum equations, except that the variables are now time averaged, and that extra terms with the fluctuating velocity components ($\overline{u_i' u_j'}$) are added. The new terms are known as the Reynolds Stresses. These terms need to be modelled for the RANS equations to be solvable, which is done through models known as turbulence models [7].

### 2.5.3 RANS based turbulence modeling

Eddy viscosity models are one category of turbulence models that are based on the Boussinesq Hypothesis, which models the Reynolds stresses by introduction of two new variables. These are the turbulent viscosity $\mu_t$ and turbulent kinetic energy $k$ [$m^2/s^2$]. See Equation 30.

$$\frac{2}{3}\rho k \delta_{ij} - \rho\overline{u_i' u_j'} = -\mu_t \left( \frac{\partial \overline{U_i}}{\partial x_j} + \frac{\partial \overline{U_j}}{\partial x_i} \right) \tag{30}$$

The goal of eddy viscosity models is to compute $\mu_t$ and $k$, enabling calculation of the Reynolds stresses. The Reynolds stresses are then put in the RANS equations which makes solving them possible. A category of eddy viscosity models are two-equation models, one being the SST $k$-omega model which is the model to be used in this thesis.

#### SST $k$-omega model

The SST $k$-omega model is a variant of the standard $k$-omega model. The $k$-omega model is based on calculating the turbulent kinetic energy $k$ and the specific turbulent dissipation rate $\omega$ [1/s]. This is accomplished through two transport equations governing the transport of these quantities [24] [25]. See Equations 31 and 32.

$$\frac{\partial \rho k}{\partial t} + \frac{\partial \rho k \overline{U_j}}{\partial x_j} = \frac{\partial}{\partial x_j}\left[ \left( \mu + \sigma_k \mu_t \right) \frac{\partial k}{\partial x_j} \right] + P_k - \rho \beta_0 f_\beta \left( \omega k - \omega_0 k_0 \right) + S_k \tag{31}$$

$$\frac{\partial \rho \omega}{\partial t} + \frac{\partial \rho \omega \overline{U_j}}{\partial x_j} = \frac{\partial}{\partial x_j}\left[ \left( \mu + \sigma_\omega \mu_t \right) \frac{\partial \omega}{\partial x_j} \right] + P_\omega - \rho \beta_0 f_\beta \left( \omega^2 - \omega_0^2 \right) + S_\omega \tag{32}$$

Where $\sigma_k, P_k, \beta_0, f_\beta, \omega_0, k_0, S_k, P_\omega$ and $S_\omega$ are model parameters. The k-omega model has been reported having problems handling certain motions in the free stream, while handling motions close to walls very well [26]. The SST k-omega variant was designed to address this by modifying the $P_\omega$ parameter in Equation 32 to include a cross-diffusion term $D_\omega$ [24]. A term $F_1$ is included in $D_\omega$ that modifies the model based on the distance to the wall in order to perform better in the free stream. Equations for $D_\omega$ and $F_1$ are presented in Equation 33 and 34, where $d$ is the distance to the wall [24] [25].

$$D_\omega = 2\rho \left( 1 - F_1 \right) \sigma_{\omega 2} \frac{1}{\omega} \frac{\partial k}{\partial x_i} \frac{\partial \omega}{\partial x_i} \tag{33}$$

$$F_1 = tanh\left( \left[ min\left( max\left( \frac{\sqrt{k}}{0.09\omega d}, \frac{500v}{d^2 \omega} \right), \frac{2k}{d^2 C D_{k\omega}} \right) \right]^4 \right) \tag{34}$$

Where $\sigma_{\omega 2}, C$ and $D_{k\omega}$ are model parameters. After solving $k$ and $\omega$ through the presented equations, the turbulent viscosity is calculated using Equation 35 according to the model [25].

$$\mu_t = \frac{k}{\omega} \tag{35}$$

With $k$ and $\mu_t$ calculated, the Reynolds stresses can subsequently be determined and the RANS equations solved.

### 2.5.4 Simulating rotating geometries

When simulating mixing processes in stirred tanks through CFD, certain methods need to be applied to simulate the rotating motion of the agitator. Two of the most common methods to simulate rotating geometries are the multiple reference frames (MRF) method and the sliding mesh (SM) method [7]. The methods are usable for any rotating geometries but will henceforth be described in the context of a stirred tank simulation.

### Multiple reference frames method

The MRF method is a steady state method and is based on dividing the computational mesh into multiple regions with different reference frames, see Figure 10. A region is created around the rotating parts, i.e. the impeller, with a reference frame that is rotating with the desired impeller speed, while the mesh itself is stationary. A stationary reference frame is instead applied to the region in the remaining space outside the rotating part region [7]. Even though different reference frames are used, the values of the flow variables are still solved with regards to the stationary reference frame.

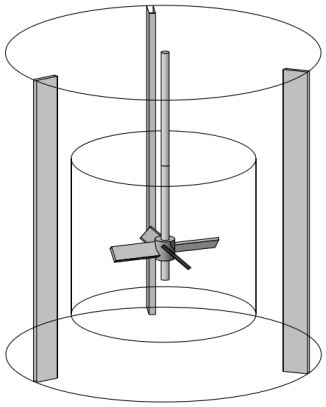

Figure 10: Stirred tank divided into a rotating region and stationary region that can have different reference frames [7]. Reprinted by permission.

An advantage of the MRF method is that it is computationally cheap. When using MRF in stirred tanks however, the impeller will be stationary since the mesh of the rotating region is stationary, meaning only one impeller position is taken into account in the simulation. This works well in a rotationally symmetric tank, where the impeller position does not affect the flow field. Using MRF is thus disadvantageous in rotationally assymetric tanks, for example in tanks with baffles or eccentrical inlets and outlets [7].

### Sliding mesh method

The sliding mesh method is a transient method, meaning it aims to simulate how the fluid motion acts over time. In the SM method, the tank is divided into rotating and stationary regions just like in the MRF method. In this method however, a motion is applied to the actual mesh of the rotating region, meaning all cells in the rotating region and the impeller is rotating. The stationary region outside the rotating region is then stationary along with the mesh [7]. This creates a need for an interpolation algorithm in the interface between the region, where the cells in the interface have varying alignment throughout a transient simulation [25]. A depiction of a sliding mesh interface between a rotating and stationary region at two different points in time is presented in Figure 11. With the SM method, the impeller blades are actually moving in the simulation, meaning the impeller blade positions are accounted for in comparison to the MRF method. Using a SM is thus often an advantage in certain simulations, for example in rotationally assymetric tanks with interactions between the impellers and baffles [7].

## 2.5.5 CFD advantages and disadvantages in mixing time prediction

The decision to use and develop a CFD method for mixing time prediction was based on CFD having several advantages over empirical and experimental methods.

### Advantages

- Flexibility with regards to tank geometry. Empirical correlations are developed for certain geometries that often perform worse in other geometries, while CFD can essentially be applied to any tank [7].
- Often cheaper and less time consuming than experimental methods.
- Enables one to be more proactive in design decisions, for example regarding what agitator is most suitable at a certain scale.

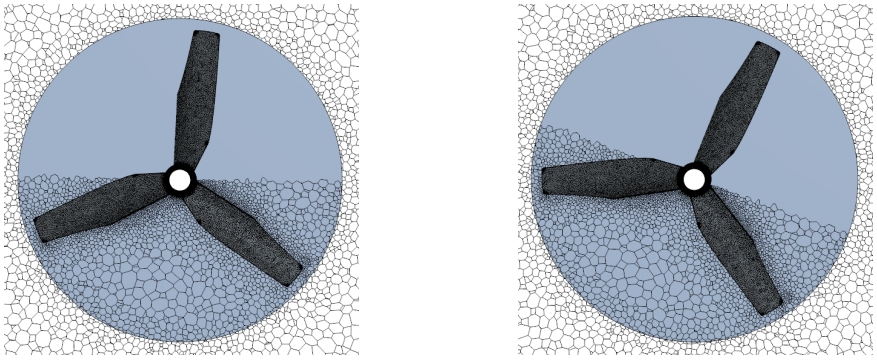

(a) (b)

Figure 11: Sliding mesh example. The blue region is rotating and the white region is stationary. Only half the mesh of the rotating region is shown to illustrate the mesh rotation.

#### Disadvantages

- Requires validation through experimental data
- The most common turbulence approach RANS is dependent on accurate turbulence models

## 2.6 Mixing time using mean age theory

CFD can be used in various ways to analyze mixing performance and predict mixing times in stirred tanks. A new CFD method using mean age theory (MAT) was proposed by Liu [8] in 2011. MAT is largely based on the concept of age, which is defined as the time a certain fluid element has spent inside a tank. Imagine a tank with an inlet and outlet, and at a certain point in time, a tagged tracer material is continuously added to the inlet. The age of the tracer fluid elements at the inlet is thus equal to zero, since that is where the material enters and has not "aged" anything yet. As the tagged tracer material fluid elements are mixed into the tank, they accumulate age, and when they reach the outlet they stop "aging" [27].

The mean age is the average age of the tracer material at a certain spatial location in the tank [27]. For example, the mean age at the inlet is equal to zero since the age of all fluid elements there are zero. The mean age in dead mixing zones may be quite high on the other hand, since the mixing there is slow and the tracer material accumulate a higher age before being flushed out of the tank. The spatial distribution of mean age in a tank thus gives valuable information of the mixing performance in different positions in the tank. Liu [8] found that the mean age distribution is related to the mixing time, and that the mixing time can be predicted by analyzing the width of the mean age distribution, which is described in detail further on in this subsection. Liu [8] and the more recent MAT author Wu [9] both used single impeller systems with an aspect ratio of 1, where Liu used a pitched blade turbine (PBT, mixed flow impeller) and Wu studied one setup with a PBT and one with a rushton turbine (RT, radial impeller).

To obtain the mean age distributions using CFD, both Liu and Wu based their model on the standard governing equation for a passive scalar, i.e. a tracer material being transported in the tank without having any physical effect on the flow [8] [9]. This makes sense intuitively since simulating the transport of tracer material enables one to determine the mean age of the tracer material throughout a tank. The general transport equation of a passive scalar is presented in Equation 36, where $D_{eff}$ accounts for the mass diffusivity, the definition of which is in Equation 37.

$$\frac{\partial C}{\partial t} = D_{eff}\nabla^2 C - \mathbf{u}\cdot\nabla C \tag{36}$$

$$D_{eff} = \left(\frac{\mu}{\rho Sc} + \frac{\mu_t}{\rho Sc_t}\right) \tag{37}$$

Where $C$ [mole/m$^3$] is the passive scalar concentration, $\mu_t$ is the turbulent viscosity, $Sc$ is the Schmidt number and $Sc_t$ is the turbulent Schmidt number. The general passive scalar transport equation can be transformed

to a mean age transport equation, meaning the mean age itself can also be solved in a CFD software, see [9] for all derivation steps. The mean age transport equation is presented in Equation 38, where $a$ [s] denotes the mean age [9].

$$\mathbf{U} \cdot \nabla a = \nabla \cdot (D_{eff} \nabla a) + 1 \tag{38}$$

MAT is a steady state approach, meaning a steady state mean age distribution is solved. Both Liu [8] and Wu [9] conducted the steady state simulations using the MRF method, and solved the flow field and the mean age distributions simultaneously. If a transient simulation is used to solve the flow field, one could instead obtain instantaneous flow fields at various time points during the simulation. This can be done by pausing the simulation and inactivating all solvers, essentially freezing the flow field. The mean age transport equation solver can then be activated. Running the simulation and thus results in a converged mean age distribution for a specific frozen flow field.

After obtaining the mean age distribution, Liu analyzed its relation to the mixing time [8]. The distribution can be represented in the form of a mean age histogram, where all mesh cells within a certain mean age span are gathered in a bin of the histogram. Liu [8] simulated different impeller speeds, and obtained the mean age histograms presented in Figure 12.

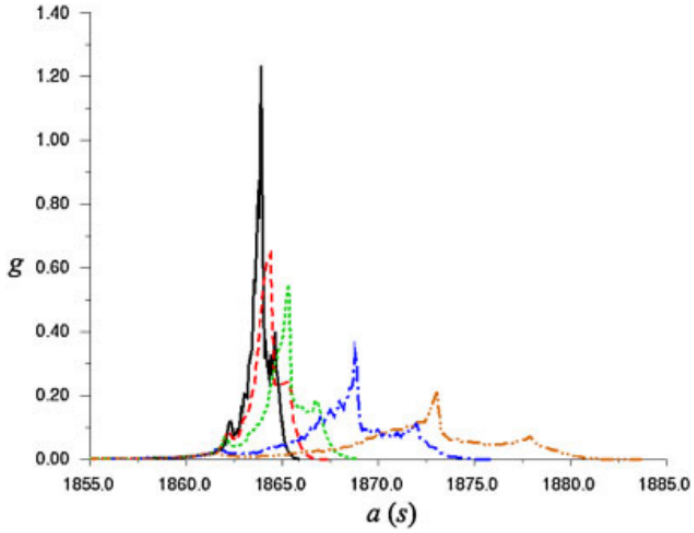


Figure 12: Liu's obtained mean age histograms at different impeller speeds [8]. The black graph represents the highest impeller speed and the orange line the slowest impeller speed. Reprinted by permission.

The mean age histogram of a theoretical ideal mixer is just a straight vertical line since it mixes the whole tank instantly, meaning all points in the tank have the same mean age. As seen in Figure 12, the mean age histograms become thinner the higher the rotation speed (faster mixing), and thus approaches the mean age histogram of an ideal mixer. Liu thus concluded that the width of the mean age histograms was proportional to the mixing time [8]. To then quantify the mixing time, Liu suggested scaling the mean age histogram. Scaling the histogram included first taking all mean ages in the distribution and subtracting the volume averaged mean age, to make all distributions have a mean of zero. The scaling also included multiplying the subtracted mean age with a factor $N$ and $\frac{D}{T}$ with varying exponents. This mean age scaling is presented in Equation 39.

$$a_s = N^{\beta} \left( \frac{D}{T} \right)^{\alpha} (a - \overline{a_V}) \tag{39}$$

Where $a_s$ is the scaled mean age, $\beta$ and $\alpha$ are scaling parameters, and $\overline{a_V}$ [s] is the volumetric average of mean age. The scaling also encompassed weighting each mean age sample (each mesh cell) with a volumetric factor to make the mean age of larger cells in the mesh have a larger impact on the mean age histogram [9]. The

volume weighting essentially turns the mean age distribution into a probability distribution function $E(a_s)$ (PDF) of mean age. This scaled mean age PDF is presented in Equation 40.

$$E(a_s) = \frac{1}{V}\frac{dv(a_s)}{da_s} \tag{40}$$

Where $v(a_s)$ [$m^3$] is the volume of tank with mean age $a_s$. An example of a scaled mean age PDF is displayed in Figure 13. Regarding the exponents $\alpha$ and $\beta$ of the mean age scaling in Equation 39, Liu used values that made the mean age PDF of different simulations, with varying conditions, come together, which turned out to be $\alpha = 2$ and $\beta = 1$. Wu [9] on the other hand used $\alpha = 0$ and $\beta = 1$, but did not specify why a different value of $\alpha$ was used, even though Wu [9] also found MAT to provide accurate mixing time predictions.

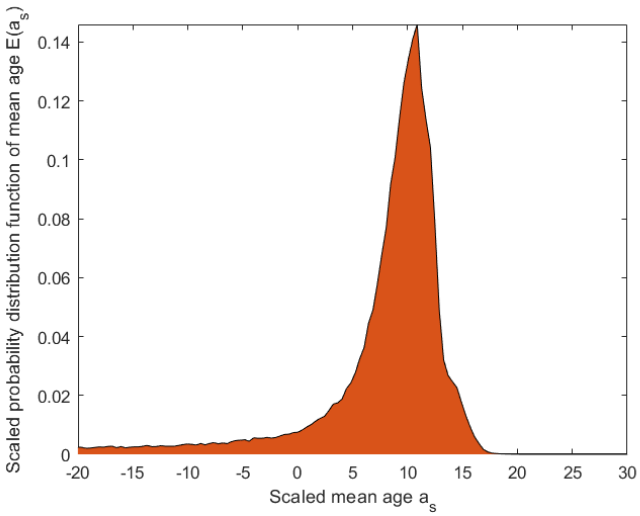


Figure 13: Example of scaled mean age PDF.

Since Liu found that the width of the mean age histograms seemed to be proportional to the mixing time, they analyzed the width of scaled mean age PDFs to quantify the proportionality between the width and the mixing time. Liu used the standard deviation $\sigma$ of the scaled mean age PDFs as a measure for the curve width. Then, since the simulations were conducted in the turbulent regime, the standard deviation were compared with two commonly used dimensionless 95 % mixing time correlations in the turbulent regime. One was Grenville's turbulence correlation presented previously (Equation 11), and the other was a correlation for a pitched blade turbine impeller. Liu found that $5\sigma - 6\sigma$ were in good agreement with the correlations, leading to the conclusion that 5 to 6 times the standard deviation of the scaled mean age PDF seems to be a good approximation of the dimensionless 95% mixing time [8]. In addition, Liu writes that a span of the mean age PDF covering a significant amount of the area is also a good approximation of the curve width and thus also the mixing time. Liu suggests integrating 95% of the area and using the integrated scaled mean age span as the approximation for $\theta_{95}$ [27].

Liu and Wu highlighted the advantage of the MAT method being a steady state method, which is significantly less computationally expensive in comparison to other CFD mixing time prediction methods [8] [9]. Another advantage is how MAT provides a complete spatial distribution of mean ages, giving information on mixing performance throghout the whole tank in comparison to other methods where only a small amount of measurement points are monitored. However, a steady state MAT method may not be suitable for setups where the impeller position has a significant impact on the flow field, since the MRF method is used. Mean age distributions are thus only obtained based on the flow field at one impeller position. Obtaining mean age distributions using a SM method may be more advantageous in this regard, which is explored in this thesis. Finally, Liu developed the MAT method based on comparison with turbulence correlations [8]. The performance of the method in transitional and laminar conditions is thus unclear, which also is explored in this thesis.

# 3 Method

This section first describes the experimental data obtained in previous work at Tetra Pak. The CFD setup is then presented, including the CFD geometry, settings and simulation method, followed by a description how the power number and impeller pumping capacities were obtained for the empirical mixing time correlations.

## 3.1 Experiments

Experimental mixing times in the tank were produced using different agitators in a separate project at Tetra Pak, where the decolorization method was used. In this thesis, CFD simulations were conducted using two of the agitators.

### 3.1.1 Experimental setups

The tank has a volume of 200 L and a conical bottom. The two agitators used in this thesis were the following:

1. **Multi-impeller system with baffles (MI setup)**. The setup includes two baffles on opposite sides in the tank and a centric agitator with three impellers mounted on a shaft, as seen in Figure 14(a). It has two upper axial impellers, pumping liquid downwards to the bottom of the tank, and a bottom radial impeller, pumping liquid radially towards the wall and later up in the tank along the walls. Dimensions are shown in Table 1.
2. **Single impeller system without baffles (SI setup)**. The setup has no baffles and includes a centric agitator with a single Viscojet impeller mounted on the bottom of the shaft, as seen in Figure 14(b). The Viscojet impeller (Figure 2(c)) has cone shaped blades pointing tangentially, and are designed with the intent to force the fluid through a smaller hole to significantly increase the fluid's velocity.

Table 1: Agitator and tank dimensions.

| **Agitator** | **D [m]** | **T [m]** | **H [m]** |
|---|---|---|---|
| MI setup | 0.25 (axial)<br>0.20 (radial) | 0.5 | 0.8 |
| SI setup | 0.19 | 0.5 | 0.8 |

### 3.1.2 Mixing time data

For both agitator setups, decolorization experiments were conducted using different fluids and agitator speeds to determine the 95 % mixing time. Three different fluids were used, one was water with Newtonian behaviour, and the other two were more viscous shear-thinning fluids. Data of the three fluids' viscosities, consistency index and flow behavior index are presented in Table 2.

Table 2: Data for the fluids used for determining the mixing times. No apparent viscosity is specified for the shear-thinning fluids.

| **Fluid** | **Type** | $\rho$ **[kg/m$^3$]** | $\mu$ **[Pa s]** | **K** | **n** |
|---|---|---|---|---|---|
| Fluid 1 | Low viscosity, Newtonian | 1000 | 0.001 | N/A | N/A |
| Fluid 2 | Medium viscosity, Shear-thinning | 1000 | N/A | 1 | 0.7 |
| Fluid 3 | High viscosity, Shear-thinning | 1000 | N/A | 11 | 0.4 |

The experiments with both agitator setups included utilization of some or all of the fluids, and a few different agitator rotation speeds. However, when simulating these mixing processes using CFD, only some of the rotation speeds were simulated due to not all being deemed necessary for the project objectives, and due to time limitations. A selection of fluids and rotation speeds was made to obtain results in a span of Reynold numbers. In Table 3, the experimental mixing time data for all experiments that were simulated using CFD is presented.

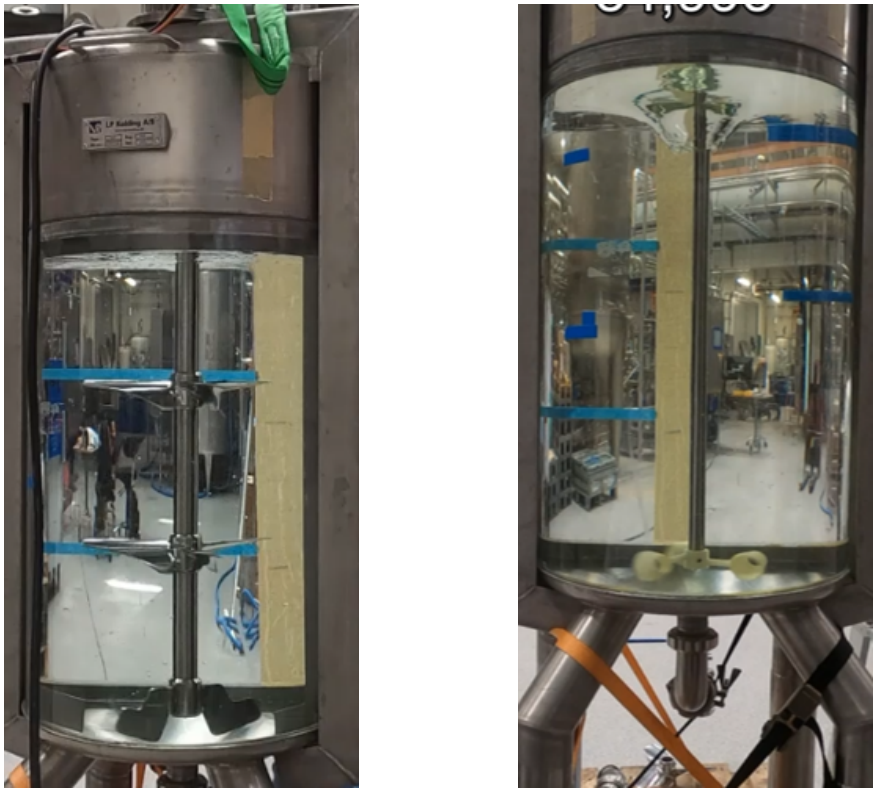

(a) (b)

Figure 14: (a) Experimental MI setup. (b) Experimental SI setup.

The agitator rotation speed was based on different tip speeds (TS) of the impellers. For the MI setup, the TS was based on the wider axial impellers, and the Reynolds number was calculated based on the diameter of the axial impeller as well. However, both impeller diameters are included in the table for clarity. See previous report at Tetra Pak for the complete data.

Calculating the Reynolds number also included calculation of the viscosity. For the shear-thinning fluids, a shear rate was approximated using the Metzner Otto method, with which the Reynolds numbers in Table 3 are based on. The proportionality constant $k_s$ was set to 12.5 since it is the value in the middle of the span 10-15 which Metzner and Otto claimed $k_s$ to be in for turbine impellers [15].

Table 3: Experimental mixing times for all agitator setups with all fluid and impeller speed combinations that were also simulated using CFD. The 95 % experimental mixing time standard deviations $\sigma_{95}$ are based on 2-3 trials.

| **Agitator** | **Fluid** | **D** [m] | **Tip speed [m/s]** | **Re** | $\theta_{95}$ **[s]** | $\sigma_{95}$ **[s]** |
|---|---|---|---|---|---|---|
| MI setup | Fluid 1 | 0.25/0.20 | 4 | 318000 | 3.4 | 0.5 |
| MI setup | Fluid 1 | 0.25/0.20 | 2 | 159000 | 7.1 | 0.8 |
| MI setup | Fluid 2 | 0.25/0.20 | 4 | 1413 | 19.2 | 2.0 |
| MI setup | Fluid 3 | 0.25/0.20 | 2 | 115 | 1330.0 | 8.4 |
| SI setup | Fluid 1 | 0.19 | 1.8 | 109000 | 34.2 | 2.9 |
| SI setup | Fluid 1 | 0.19 | 0.6 | 36000 | 233.3 | 25.2 |

## 3.2 CFD setup

### 3.2.1 CFD geometry

A 3D-CAD model and mesh of the MI setup had already been produced previously at Tetra Pak which was utilized in this thesis. For the SI setup, a 3D-CAD model existed but no mesh had been generated. The SI setup mesh was generated by another employee at Tetra Pak based on knowledge from the MI setup mesh generation.

All geometries in the project were separated into static and rotating regions. The rotating regions cylinders that covered the impellers were simulated using either the MRF or SM method. For the MI setup, a rotating region was created for each impeller resulting in three rotating regions in total, as seen in Figure 15(b), whereas the SI setup only had one rotating region, as seen in Figure 15(d). The static region consisted of the remaining parts of the tank, including the walls, shaft, top and bottom, as well as the baffles in the case of the MI setup. The geometry and the rotating regions for the MI and the SI setups are displayed in Figure 15.

The geometry has an eccentric inlet at the top of the tank and a centric outlet at the bottom for the tracer material, which was required to obtain the tanks' mean age distributions with MAT [9]. The inlet was placed at approximately the same location as the inlet of the decolorization agent in the experiments.

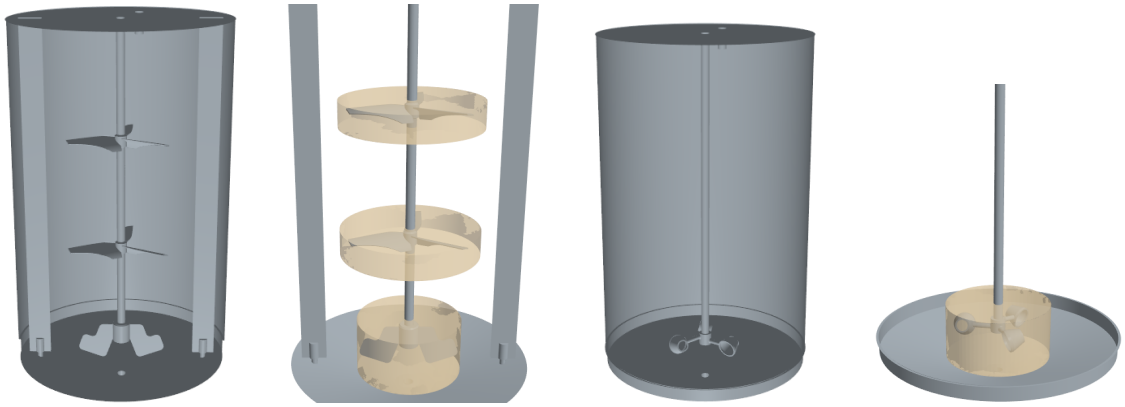

(a) (b) (c) (d)

Figure 15: (a) MI setup geometry (b) MI setup rotating regions (c) SI setup geometry (d) SI setup rotating region

### 3.2.2 Simulation settings

All simulations, with varying agitator, fluid and tip speed, were initiated by a steady state simulation using the MRF method. The converged steady state field was then used as the initial conditions for a transient simulation using the SM method. Following the transient simulation, the flow field was frozen at various instants to be used in mean age simulations.

The general physics settings were set up the same way as in previous work at Tetra Pak where the MI setup was simulated. The SST k-omega turbulence model in particular had been shown to work better for similar mixing processes in work done by previous master's thesis students [28] [29]. A previous time step study also motivated the specific time step used in the transient simulations. Fluid properties and rotation rate of the rotating regions were specified in accordance with the experiments the simulations are aimed to resemble, see Table 3. The shear-thinning fluids' viscosities were specified using the power law.

The mean age was modeled as a passive scalar in the mean age simulations. Specification of the molecular Schmidt number and turbulent Schmidt number determines the rate of diffusion of the passive scalar. A value of 672.0 was chosen for the molecular schmidt number in agreement with Wu's [9] model, whereas a slightly lower value (0.7) than the default value was chosen for the turbulent Schmidt number, since Liu [8] did the same and obtained satisfactory results in a similarly sized tank.

For the transient simulation, the remesher setting was activated with all options unchecked in the settings

tree. The remesher was needed to obtain time averaged flow fields, which was part of the objective with the transient simulation. This is further described in subsection 3.2.4.

In summary, the physics were set up in accordance with Table 4.

Table 4: Physics

| Setting | Chosen option/value |
|---|---|
| **General** | |
| Equation of state | Constant density |
| Turbulence model | SST k-omega |
| Wall treatment | All y+ |
| Transition model | Gamma transition |
| Solver type | Segregated |
| Gradients | Activated |
| Solution interpolation | Activated |
| **Transient simulation** | |
| Implicit unsteady | Activated |
| Remesher | Activated |
| **Passive scalar** | |
| Molecular Schmidt number | 672.0 |
| Turbulent Schmidt number | 0.7 |
| Passive scalar URF | 1.0 |
| **Solver** | |
| Time step | 2 degrees rotation per time step |
| Flow solver algorithm | SIMPLE |
| **Stopping criteria** | |
| Inner iterations | 7 |

### 3.2.3 Boundary conditions

The boundary between the rotating regions and the static region was a region interface, the behaviour of which was greatly affected by whether an MRF or SM method was used. During the initial steady state MRF simulation, the mesh was stationary, while In the transient simulation, the mesh of the rotating region was rotating.

On the top of the tank, a slip wall boundary condition was imposed to reflect the liquid surface in the tank. For the side walls, baffles, shaft, bottom and impeller blades, a wall no-slip boundary condition was set since these surfaces are solid. At the inlet and outlet, an inlet mass flow and outlet mass flow condition were applied, respectively. The decision to set the outlet to mass flow instead of pressure outlet was based on observations of backflow when using the pressure outlet condition. Both the inlet and outlet boundary conditions were set to a sufficiently low mass flow rate $q$ for them to not affect the overall flow in the tank, which is essential since the physical tank is a batch tank. The mass flow rate $q$ was set to 0.02 kg/s since Liu [8] determined that $q < 0.02$ kg/s had a negligible effect on the flow field in a similarly sized tank. Finally, a wall relative rotation motion was applied to the agitator shaft in accordance with the rotation speed, since the shaft is rotating as well.

A summary of the boundary conditions is presented in Table 5

### 3.2.4 Transient simulations

Again, simulations were conducted using the agitators, fluids and tip speeds presented in Table 3. Throughout the transient simulation, data needed for mixing time prediction was gathered and obtained. This is described further in upcoming sections. Additionally, after completing the transient simulation, various instantaneous flow fields were obtained, frozen and used for mean age simulations and subsequent mixing time predictions.

Table 5: Boundary conditions

| Surface | Boundary condition |
|---|---|
| Top | Wall. Slip. |
| Side walls, bottom, baffles, shaft, impeller blades | Wall. No slip. |
| Inlet | Inlet mass flow. 0.02 kg/s |
| Outlet | Outlet mass flow. 0.02 kg/s |

Besides the instantaneous flow fields, it was also desirable to analyze how the field generally behaved over time. This was done by time averaging the flow field and all solved flow variables throughout the transient simulation. The time averaged flow field data was obtained as a separate field and could also be used in mean age simulations for comparison with the mean age simulations using instantaneous flow fields. See Appendix A for details on how the time averaged flow fields were obtained.

The transient simulations were conducted until the flow field was considered to be fully developed, i.e. when the initial transient behavior no longer seem to have an effect on the flow variables, meaning the flow is stabilized and has developed hydrodynamic conditions. A fully developed flow field was desired for proper determination of the mixing time without the initial transients affecting the predictions. Also, the project scope covers only these fully developed mixing processes, and the experimental mixing times are produced under fully developed flow conditions as well. For determination of when the flow field was considered fully developed, measurement points were set up in the tank model, see Figure 16. The velocity magnitude at these points was monitored at every time step and analyzed for determination of a fully developed flow field. The points were positioned to obtain a satisfactory spread of the velocity magnitude measurements by setting the bottom four ones in the discharge regions of the impellers and the top four ones close to the liquid surface where mixing is slower.

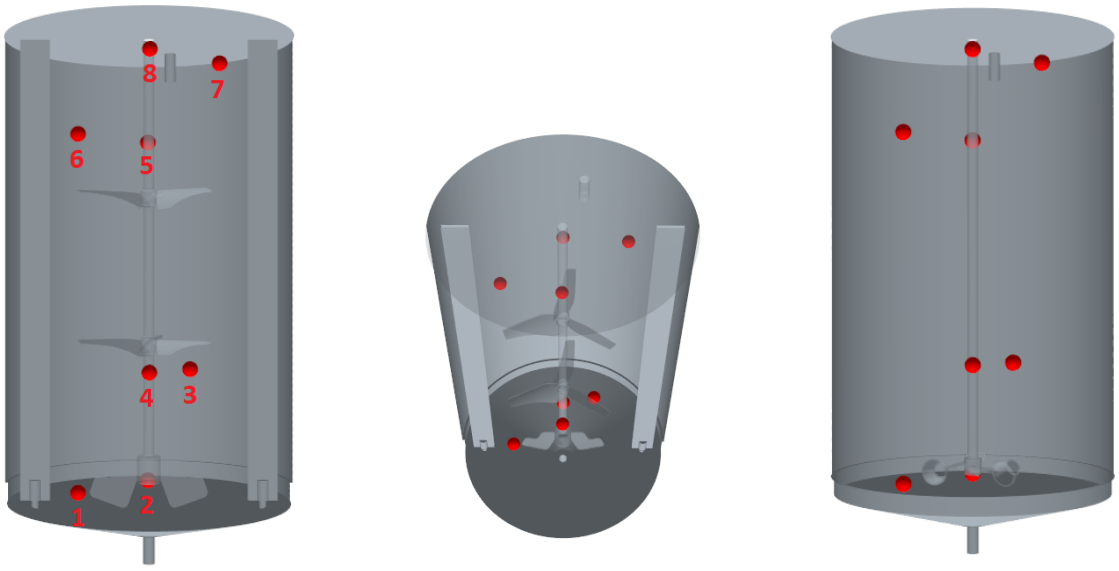


(a) (b) (c)

Figure 16: Velocity magnitude measurement points. (a) MI setup view 1 with point labels (b) MI setup view 2 (c) SI setup

### 3.2.5 Mean age simulations

After the transient simulations, the mean age simulations were conducted, and the CFD method based on MAT was developed and analyzed.

### Frozen flow fields

MAT authors Liu [8] and Wu [9] both used a steady state MRF method to obtain the flow field, and they solved the mean age equation simultaneously. Our decision to focus on the SM method was based on its superiority in capturing impeller-baffle interactions, as described in subsection 2.5.4. Since MAT is a steady state approach, various frozen flow fields were obtained from the transient simulation using which steady mean age distributions could be produced. For each simulation, several instantaneous flow fields were frozen and used in steady mean age simulations until a converged mean age distribution was obtained. The time averaged flow field obtained for each transient simulation was used in a mean age simulation as well.

### Mean age distribution analysis

As described in subsection 2.6, Liu [8] and Wu [9] scaled the mean age distribution using different $\alpha$ in the scaling presented in Equation 39. Thus, we decided to try different $\alpha$ in the scaling to which best predicted the experimental mixing time data.

Liu [8] suggested different ways to approximate the scaled mean age PDF curve width for the mixing time prediction, and we decided to generally focus on one of them. The approach was to approximate the width as the span over which the area of the PDF curve reached a certain level. See Figure 17 where 95 % of the area under the PDF curve is integrated.

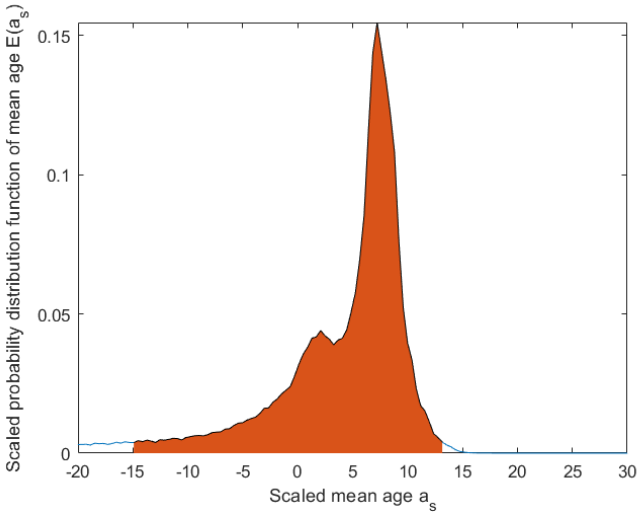


Figure 17: Mean age PDF example with 95 % area integration

## 3.3 Empirical mixing time correlations utilization

### 3.3.1 Power number calculation

In order to predict the mixing time using the power number correlations described in subsection 2.4, the impeller torque needed to be calculated for each simulation. This was done by integrating the pressure and the shear stress on the impeller blades at each time step, thus monitoring the torque throughout the simulation. For the MI setup, the torque was monitored for each impeller separately. Subsequently, the power input of each impeller was calculated through Equation 41 presented below.

$$P = 2\pi N \Lambda \tag{41}$$

The power numbers were then be determined according to Equation 2. For the MI setup, the power number of the three impellers were summed to obtain a total power number to be used in the Grenville and Cooke correlations. In the Magelli correlations, averages of the three power numbers were used as approximation of an individual power number, since individual power numbers were used in development of the correlation.

### 3.3.2 Circulation time calculation

In order to calculate the flow number and use the circulation time correlation, the pumping capacity of each impeller was determined. In accordance with the method described in subsection 2.1.4, this was done by integrating the velocity perpendicular to a surface covering the pumping direction of each impeller. For the MI setup, the radial velocity was integrated over a cylinder surface surrounding the radial impeller to determine its pumping capacity, as was done for the SI setup impeller. For the axial impellers of the MI setup, the velocity vector downwards in the tank was integrated over a circle just below each axial impeller. These surfaces are depicted in Figure 18.

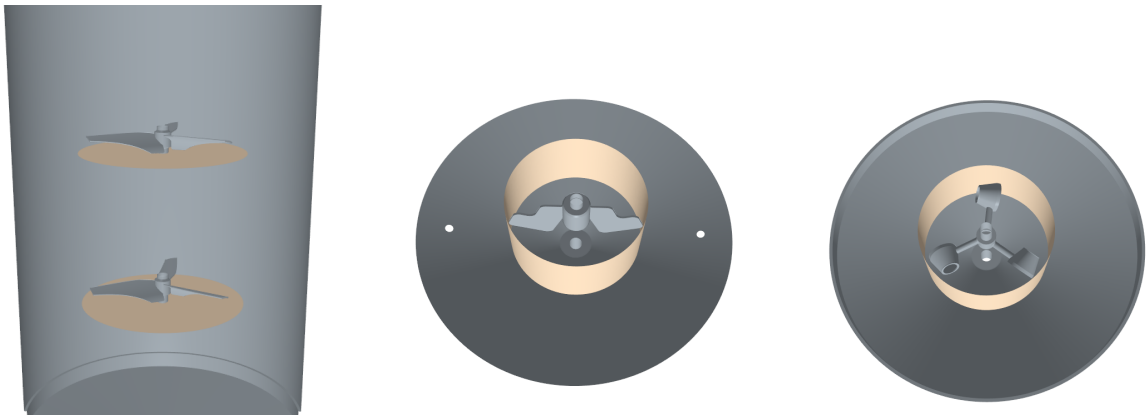

(a) (b) (c)

Figure 18: Surfaces created for measurement of impeller pumping capacity. (a) MI setup axial impellers (b) MI setup radial impeller (c) SI setup

The circulation time was then calculated using equation 4, where the pumping capacity for the lower axial impeller was used as a measure for the volumetric tank flow in the MI setup. Subsequently, the mixing time was predicted using the circulation time correlation (Equation 17).

# 4 Results and Discussion

The results for each agitator setup will be presented one at a time, starting with the MI setup. The results will also be presented and analyzed for each flow regime separately starting with the turbulent regime, followed by the transitional and laminar regime. As described previously, all simulations were conducted using the fluids and tip speeds presented in Table 3, and all transient simulations were initialized using a converged steady state flow field obtained using the MRF method.

## 4.1 Multi-impeller setup

### 4.1.1 Turbulent regime simulations

Two tip speeds, i.e. 4 m/s and 2 m/s, were simulated in the turbulent regime using Fluid 1 (Newtonian low viscosity).

#### Transient simulations

As described in subsection 3.2.4, during the transient simulations, the velocity magnitude was tracked at the eight spread out measurement points in the tank. These velocity magnitude measurements were time averaged throughout the transient simulations to determine when the flow field could be considered to be fully developed. The time averaged velocity magnitudes for both turbulent simulations are presented in Figure 19.

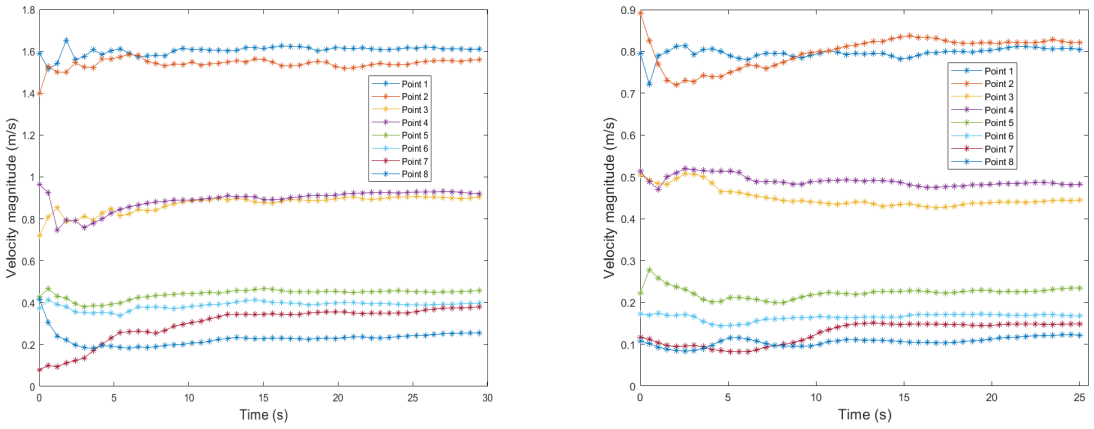


Figure 19: Time averaged velocity magnitudes at eight measurement points. Low viscosity simulations. (a) 4 m/s TS (b) 2 m/s TS

When the time averaged velocity magnitudes are stabilized and the graphs become planar, one can quite confidently draw the conclusion that the initial transient no longer has any major influence on the flow field, meaning the flow field is developed. As is seen in the figure, this seems to have occurred after simulating for 12.5 seconds for the 4 m/s TS and after 17.5 seconds for the 2 m/s TS. Note that the measurement points are distributed at four different tank levels and that points 7 and 8 are close to the tank top where the flow is expected to develop the slowest. A reasonably good spatial spread of the velocity magnitude measurements is thus achieved, which is necessary for determination of the developed flow field.

Time averaged velocity profiles at two different vertical planes for both turbulent simulations are depicted in Figure 20, where plane 1 is in line with the baffles and plane 2 is perpendicular to plane 1. The displayed velocity considers only axial and radial components. Henceforth, this is the velocity that is referred to in corresponding velocity profiles for other simulations if nothing else is stated.

The time averaged profiles demonstrate the synergy of the impellers, where the axial impellers pumps liquid down to the radial impeller which distributes the liquid radially and up along the walls. The baffles also likely aids significantly in achieving the observed vertical flow necessary for good mixing. We also see how the velocities are reduced at the lower tip speed as expected, but retains the general flow profile. Additionally,

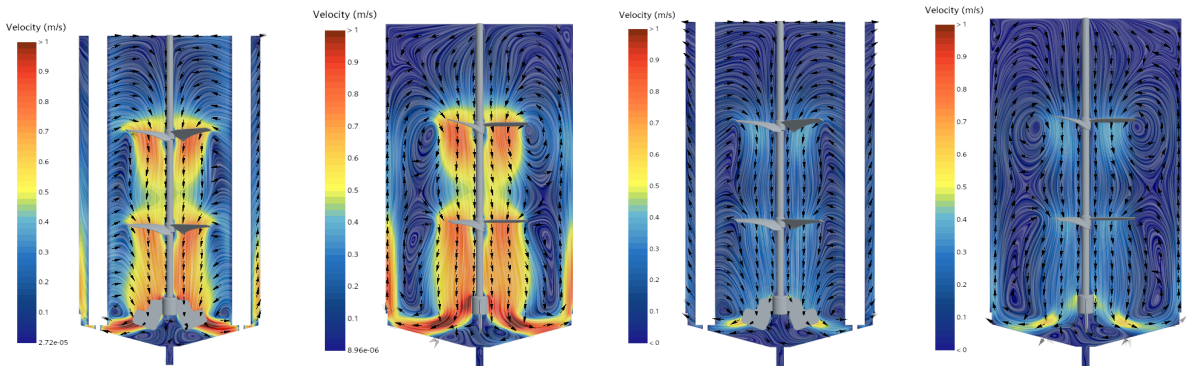


(a) (b) (c) (d)

Figure 20: Time averaged velocity profiles. Low viscosity simulations. (a) Plane 1, 4 m/s TS (b) Plane 2, 4 m/s TS (c) Plane 1, 2 m/s TS (d) Plane 2, 4 m/s

the flow profile demonstrates how the combination of multiple impellers and baffles work together to achieve a satisfactory mixing pattern in this tank with a high aspect ratio.

### Mixing time prediction using empirical methods

To use the empirical mixing time turbulence correlations based on the power number and circulation time, the torque and impeller pumping capacity were calculated as described in subsection 3.3. These parameters varied and oscillated slightly due to the transient nature of mixing processes. Therefore, a time averaged value was calculated for these parameters towards the end of the simulation when the flow was developed. The same procedure was done for all simulations in this thesis.

Mixing time predictions using empirical correlations developed in the turbulent regime (see subsection 2.4) and corresponding experimental mixing times are presented in Table 6. The correlation names are shortened for improved readability.

Table 6: Mixing time predictions for the MI setup using empirical correlations developed in the turbulent regime.

| **Fluid** | **Tip speed [m/s]** | **Re** | **Grenville $\theta_{95}$ [s]** | **Cooke $\theta_{95}$ [s]** | **Magelli NZ $\theta_{95}$ [s]** | **Magelli WZ $\theta_{95}$ [s]** | **Circulation time $\theta_{95}$ [s]** | **Exp. $\theta_{95}$ [s]** |
|---|---|---|---|---|---|---|---|---|
| Fluid 1 | 4 | 318000 | 3.7 | 7.9 | 19.4 | 6.5 | 20.8 | 3.4 |
| Fluid 1 | 2 | 159000 | 7.5 | 15.8 | 39.1 | 13.0 | 40.3 | 7.1 |

The Grenville correlation [15] clearly makes the most accurate mixing time predictions. This suggests that the MI setup to a certain extent has a similar behavior as the single impeller systems used by Grenville in the development of his correlation, even though the MI setup is taller with an aspect ratio of 1.6 compared to the ratio 1.0 used by Grenville. One could argue that the inclusion of two axial and one radial impeller gives the tall MI setup a flow pattern that resembles that of a single axial impeller, which can observed by comparing Figure 20 and Figure 3. This could partly explain the high performance of the Grenville correlation.

The Cooke correlation [30] predictions are roughly twice as large as the experimental mixing times, which is expected to some extent due to the appearance of the zoning effects when developing the correlation, as written in subsection 2.4. No zoning effects are observed in the turbulent flow profiles in the MI setup due to the use of both axial and radial impellers, which could explain the discrepancy between the predictions and the experiments. Better predictions are likely achieved in setups with zoning effects.

The mixing time overpredictions of Magelli's correlations [20] are likely due to them being based on systems with multiple identical non-interacting impellers, as described in subsection 2.4. In the MI setup, there are two different impeller types (non-identical) that seem to be interacting based on the presented time averaged flow fields. A constructive interaction between the impellers is expected to decrease the mixing time in comparison

to completely non-interacting impellers. Magelli's correlations could be more useful in future work analyzing systems with multiple non-interacting impellers. However, it is also quite unexpected that the NZ Magelli correlations performs significantly worse than the WZ correlation, since no zoning effects are observed in the MI setup. In addition, the considerably lower mixing time using the WZ correlation is quite odd in itself, since zoning effects would arguably increase the mixing time. It does however agree with Magelli's study, where the data from zoning configurations generally had lower mixing times [20], explaining the lower prediction of the WZ correlation. We did not find any comment by Magelli regarding these findings. Generally, this discussion highlights the importance of studying correlations properly to understand when they can be applied and utilized and when they cannot. This is especially true for these more complex multi-impeller setups.

Another important aspect to keep in mind when applying all empirical correlations in multi impeller systems is which impeller diameter to base the correlation calculations on, since the axial and radial impellers of the MI setup have different diameters, whereas all presented correlations were developed using a single impeller diameter. How to handle different impeller diameters is not studied in the researched literature. We found that using the axial impeller diameter generally resulted in the most accurate mixing time predictions, leading to us basing all correlations on the axial impeller diameter.

The high mixing time prediction using the circulation time correlation suggests that it is not suitable in turbulent conditions using the MI setup.

### Frozen flow fields

Different frozen flow fields were obtained from the developed flow field to be used in the steady state mean age simulations, and a majority of them were instantaneous flow fields frozen at various time points. It was first hypothesized that the impeller position at which the flow field was frozen would have a significant impact on the mixing time predictions, since the impeller blades have different positions in relation to the inlet and the baffles. Therefore, flow fields were frozen and saved at impeller positions 30 or 60 degrees rotation between each for a whole rotation. The same procedure was conducted at two more time points after around 3 and 6 additional simulated seconds, resulting in three total samplings. Mixing times were then predicted through mean age simulations and MAT using all the frozen flow fields. Mixing time predictions for the three samplings are presented in Figure 21.

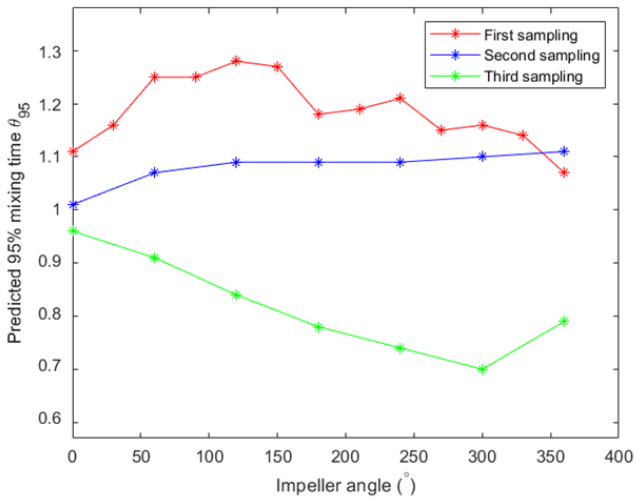


Figure 21: Scaled mixing time predictions for using flow fields frozen at different impeller angles for three samplings. The mixing times are scaled by dividing all mixing times with the value of the second sampling at impeller angle = 0 to display the relative differences. Angle = 0 refers to the position where the blades of the radial impeller is in line with the baffles.

The figure shows that the impeller position does not seem to have a major impact on the mixing time prediction. Instead, the predictions seem to be affected by the time points at which the frozen flow fields are sampled. Therefore, we decided to switch the sampling method to instead obtain frozen flow fields at the same impeller

angle but at different time points. The first instant flow field was frozen directly after finishing the transient simulation with the radial impeller blades in line with the baffles. Then, the transient simulation was resumed and run for another three impeller rotations, after which another instant flow field was frozen. The procedure was repeated an additional three times, resulting in five sampled instant flow fields with three simulated impeller rotations between each. These will henceforth be referred to as samples 1-5. This sampling provides more information on the variation of the predicted mixing times over a longer time span. In addition to the instant flow fields, the time averaged flow field for each transient simulation was also used in a mean age simulation. Corresponding frozen flow fields were used in simulations with the other fluids, tip speeds and the SI setup.

### Mean age simulations and distributions

Two obtained instant velocity profiles, the time averaged velocity profile and corresponding mean age distribution profiles for the 4 m/s tip speed are shown in Figure 22. All sample profiles for both the 4 m/s TS and 2 m/s TS simulations are found in Appendix B.

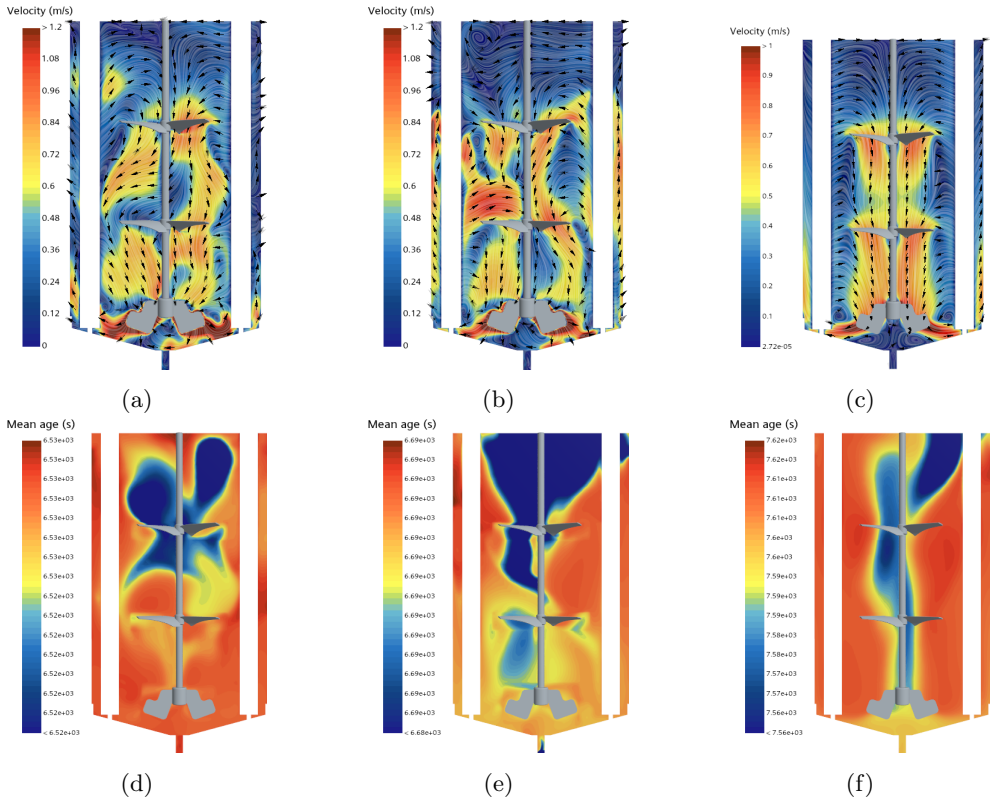


Figure 22: Velocity profiles for two instant flow fields and time averaged flow field, and corresponding mean age profiles. Low viscostiy simulation with 4 m/s TS. (a) & (d): Sample 1. (b) & (e): Sample 5. (c) & (f): Time averaged

Qualitative analysis can be conducted using the presented mean age distributions. For example, the low mean age in the top right parts of the mean age plots represents the inlet, where passive tracer material enters the tank and thus have a low age. This is likely connected to the spirally formed area in the middle of the time averaged mean age field, where some tracer material from the inlet is mixed into the upper axial impeller flow and pumped down in the tank, resulting in a lower mean age in the middle of the tank, generally suggesting fast mixing in the middle of the tank and worse along the walls and at the top. Observing the instant profiles in Figure 22(b) and (e) on the other hand would suggest fast mixing in the top of tank compared to the rest, which would could indicate compartmentalization. The other instant profiles in Figure 22(a) and (d) indicate that the top axial impeller does most of the mixing. These observations are seemingly quite odd suggesting that the instant profiles are not suitable when interpreting the general flow profile and mixing performance of the tank. The time averaged profile is more suitable in this regard, and is also more relevant since it is averaged for all impeller positions.

As described in subsection 3.2.5, the mean age distributions were scaled and transformed into scaled mean age PDFs to quantify the mixing time. Initially, 95 % of the PDF area was integrated as a measure of the curve width for prediction of the mixing time, as was done by Wu [31]. Scaled mean age PDFs for the previously presented distributions with 95 % integrated area are shown in Figure 23. All scaled mean age PDFs for both the 4 m/s TS and 2 m/s TS simulations are found in Appendix B.

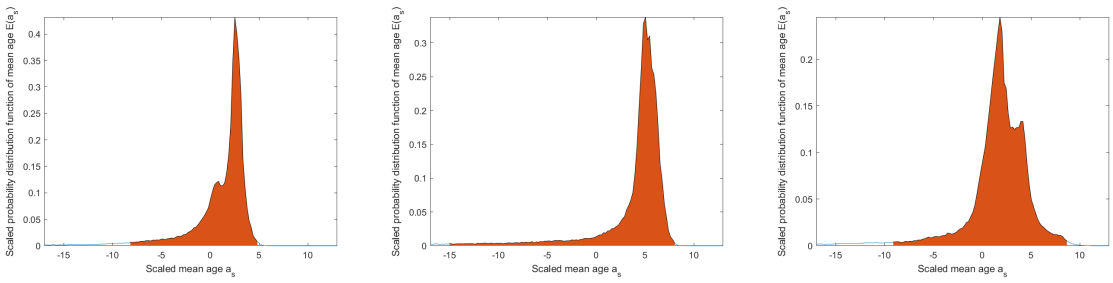


(a) (b) (c)

Figure 23: Scaled mean age PDFs using $\alpha = 2$ for two instant flow fields and the time averaged flow field. Low viscosity simulation with 4 m/s TS. (a) Sample 1 (b) Sample 5 (c) Time averaged

### Mean age PDF scaling and mixing time predictions

Liu [8] used $\alpha = 2$ in the PDF scaling (Equation 40) and Wu [9] used $\alpha = 0$. We thus decided to investigate scalings with four different $\alpha$-values in this interval, i.e. 0, 0.5, 1.0 and 2.0. All instant and time averaged mean age distributions were scaled with all four scalings. The resulting mixing time predictions for both turbulence simulations are presented in Figure 24.

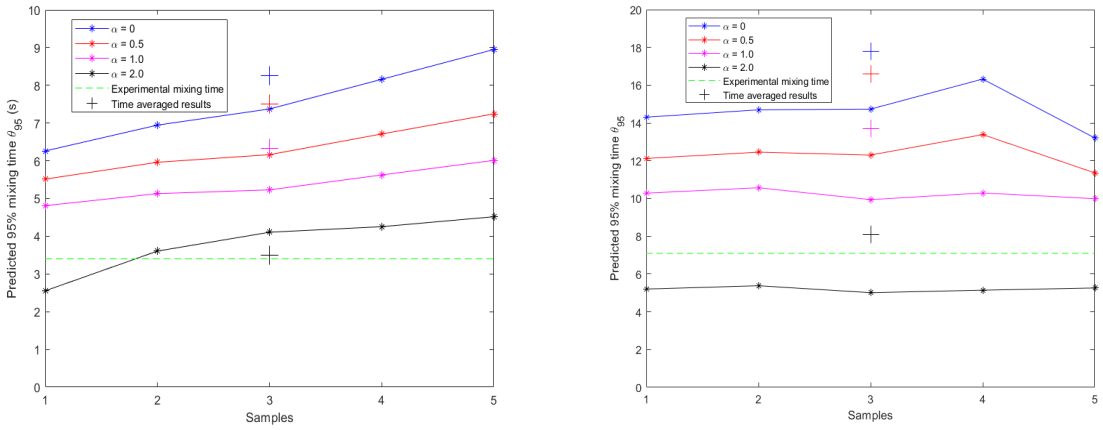


(a) (b)

Figure 24: Mixing time predictions for five instant flow field samples and time averaged flow field, using four different mean age scalings and 95 % PDF area integration. Low viscosity simulations. (a) 4 m/s TS (b) 2 m/s TS

As is seen in Figure 24, mixing time predictions decrease with increasing scaling exponent $\alpha$. This essentially means that decreasing the exponent makes the mean age PDF curve more narrow. Using $\alpha = 2.0$ seems to give the best predictions, which agrees with Liu's results where the same scaling was used. This scaling is thus the one used for the PDFs displayed in Figure 23. We also see that using the time averaged flow field seems to give the most accurate predictions, suggesting it is the most appropriate flow field to use in these turbulent simulations. Besides, the instant flow fields show quite a bit of variation, especially for the 4 m/s TS simulation. This can be understood by studying the scaled mean age PDFs for the instant flow fields in Figure 23, where we see that the curves are unexpectedly "smoothed out", especially the left side of the

curves. Because of this, the width of the integrated area becomes quite sensitive to variations in the mean age distributions, and significant variations are clearly observed in the PDFs seen in Figure 23 and in Appendix B. Additionally, having such sensitivity is generally undesired since it creates a need for more instant flow field samples to calculate an average from if more confident predictions are to be made. Finally, a physical argument can be made in favor of using the time averaged flow field as well. The experimental mixing time is measured over a time span while the agitator is continuously mixing, and not using some specific instant flow field. Using a time averaged flow field provides more information on the system's behavior over time and thus gives a more physically accurate representation in relation to the experiments.

Nonetheless, using instant flow fields still aid in providing a broader analysis. For example, it is quite odd that the time averaged results for the 2 m/s TS simulation are significantly higher than the instant flow field results, as observed in Figure 24. One would on the other hand expect that the average of the different samples would come closer to the time averaged results. Also, using instant flow fields at different impeller positions can be valuable in cases where the impeller position has a larger impact, which is not the case for these turbulent simulations.

Regarding the mean age PDF scaling, it is seemingly odd that Wu [9] used a different scaling than Liu [8] without commenting or discussing it, since our results demonstrate the major impact of the choice of scaling. For example, our results show a three to four times larger mixing time prediction for $\alpha = 0$ than $\alpha = 2.0$. Nevertheless, our predictions clearly performs best using Liu's scaling who initially developed the MAT method. This agreement is quite interesting since Liu (and Wu) used a shorter tank with a single PBT. Also, recall that Liu developed the mean age PDF width relation based on turbulence correlations that were also produced using single impeller systems similar to Liu's and Wu's, one of which was Grenville's turbulence correlation. As showed previously, Grenville's correlation gave satisfactory mixing time predictions in the turbulent regime. Liu's MAT method could thus be argued to perform well in the MI setup for the same reasons that Grenville's correlation seems to work well. A comparison is made in Table 7 where mixing time predictions using Grenville's correlation and MAT are presented. For MAT, both the time averaged results and a mean of the instant flow field samples are presented.

Table 7: Mixing time predictions using Grenville's turbulence correlation, MAT with time averaged field, and MAT with mean of instant flow field predictions. MAT predictions are based on the $\alpha = 2.0$ scaling.

| **Fluid** | **Tip speed** [m/s] | **Re** | **Grenville** $\theta_{95}$ [s] | **MAT time avg** $\theta_{95}$ [s] | **MAT instant mean** $\theta_{95}$ [s] | **Exp.** $\theta_{95}$ [s] |
|---|---|---|---|---|---|---|
| Fluid 1 | 4 | 318000 | 3.7 | 3.5 | 3.8 | 3.4 |
| Fluid 1 | 2 | 159000 | 7.5 | 8.1 | 5.2 | 7.1 |

The table demonstrates especially the similar predictions using Grenville's correlation and MAT time averaged results.

A remark should also be made regarding the different CFD approaches used in this thesis versus in Liu and Wu's studies. They both used the k-epsilon turbulence model which may account for differences in our results versus theirs. No sensitivity analysis was however conducted with regards to the turbulence model in this thesis. Additionally, Liu and Wu relied solely on the MRF method whereas we used frozen flow fields from a SM simulation.

### 4.1.2 Transitional regime simulation

One tip speed, i.e. 4 m/s, was simulated in the transitional regime using Fluid 2 (non-Newtonian medium viscosity).

#### Transient simulation

The time averaged velocity magnitudes of the measurement points used to determine a fully develop flow field is shown in Figure 25. Again, the flow field appears to be developed after 25 simulated seconds. Time averaged velocity profiles at the two perpendicular planes are depicted in Figure 26.

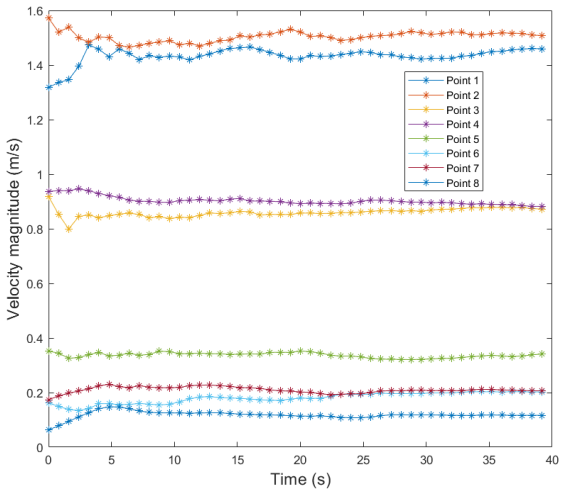


Figure 25: Time averaged velocity magnitudes at eight measurement points. Medium viscosity simulation with 4 m/s TS.

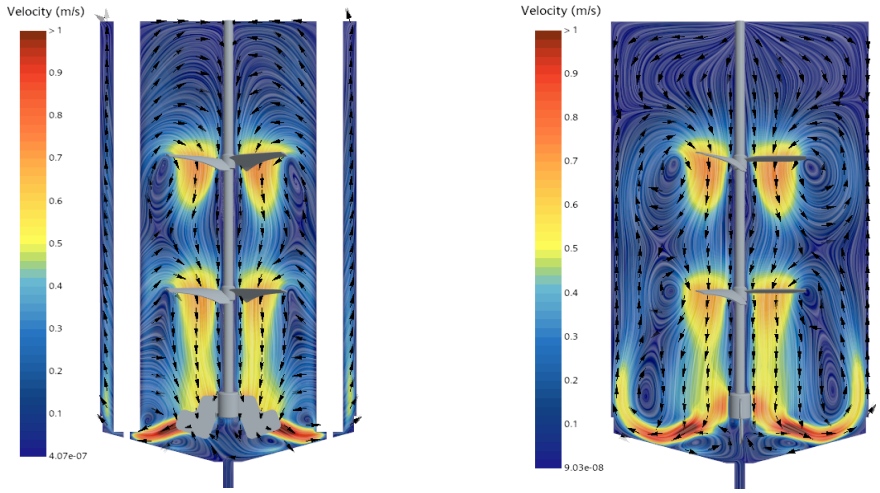


(a) (b)

Figure 26: Time averaged velocity profiles. Medium viscosity simulation with 4 m/s TS. (a) Plane 1 (b) Plane 2

The time averaged velocity profile generally looks similar to the turbulent 4 m/s TS profile, except with lower velocity magnitudes which is expected when using a more viscous fluid. In Figure 26(a) we also observe two recirculation zones under the upper axial impeller which were not observed in the turbulent simulations.

### Mixing time prediction using empirical methods

In order to use Grenville's transitional correlation, a Reynolds number at the wall was determined using the methodology described in subsection 2.4.2. A sum of the three impeller torques were used in the equations, since Grenville used a single impeller system. Besides Grenville's, the circulation time correlation was the only other correlation used in the transitional regime. Even though it was generally developed in the turbulent regime, we decided to analyze its performance in the transitional and laminar regime as well. Magelli's and Cooke's correlations were clearly only applicable in the turbulent regime and were thus not used. Mixing time predictions using the empirical correlations are presented in Table 8.

Just like in the turbulent case, we see that Grenville's correlation performs quite well in the MI setup, even

Table 8: Mixing time predictions using Grenville's transitional regime correlation and the circulation time correlation

| **Fluid** | **Tip speed [m/s]** | **Re** | **Grenville $\theta_{95}$ [s]** | **Circulation time $\theta_{95}$ [s]** | **Exp. $\theta_{95}$ [s]** |
|---|---|---|---|---|---|
| Fluid 2 | 4 | 1410 | 14.6 | 28.1 | 19.2 |

though it gives a worse prediction compared to the turbulent case. As in the turbulent simulations, we again used the larger axial impeller diameter when applying Grenville's correlation. However, if instead the smaller radial impeller diameter was used, we would obtain a higher mixing time since $D$ is in the denominator (see Equation 18), which would be a more accurate prediction since it currently is underpredicted. Additionally, Grenville and Nienow [15] does not discuss how to calculate the Reynolds number at the wall for multi-impeller systems. Summing the impeller torques is just an approximation deemed reasonable in this thesis.

Regarding the circulation time correlation, it is observed to provide a better prediction than in the turbulent regime, but still significantly overpredicts the mixing time. Thus, it does not seem to suitable for the MI setup in the transitional regime either.

### Mean age simulations and distributions

Two instant flow profiles, time averaged flow profiles and corresponding mean age distribution profiles are presented in Figure 27. All samples profiles and the connected scaled mean age PDFs are shown in Appendix B.

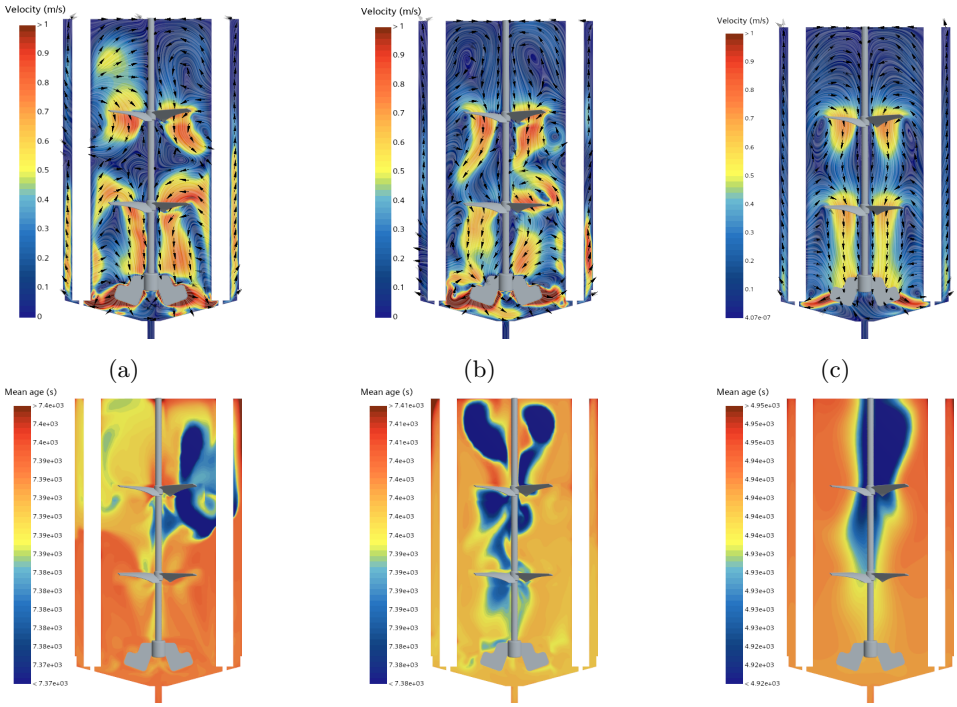


Figure 27: Velocity profiles for two instant flow fields and time averaged flow field, and corresponding mean age profiles. Medium viscosity simulation with 4 m/s TS. (a) & (d) Sample 1. (b) & (e) Sample 5. (c) & (f) Time averaged

Just like in the turbulent case, the instantaneous mean age profiles are arguably less relevant and has more unrealistic interpretations. Also, as seen in the figure, their variation between different time points makes it difficult to draw general conclusions about the mixing performance. The time averaged profile is quite similar to the turbulent one, especially with regards to the low mean age spread from the inlet and down in the middle

of the tank. A larger mean age difference is however observed between the bottom and the top and corners of the tank, suggesting the top and corners of the tank are being mixed more slowly which is expected.

### Mean age PDF scaling and mixing time predictions

Mixing time predictions for the five instant flow fields and time averaged flow field using the four different PDF scalings are presented in Figure 28.

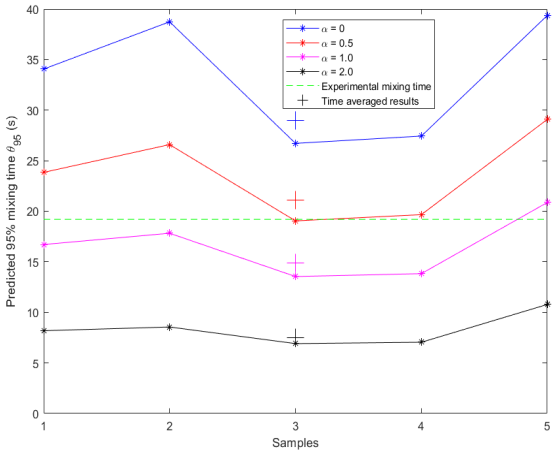


Figure 28: Mixing time predictions for five instant flow field samples and time averaged flow field, using four different mean age scalings and 95 % PDF area integration. Medium viscosity simulation with 4 m/s TS.

Clearly, the method is unable to predict the mixing time in when using the original scaling with $\alpha = 2.0$. This suggests that it is not suitable to directly apply Liu's methodology in the transitional regime, which is reasonable since he developed it in the turbulent regime. As is seen in Figure 28, using $\alpha = 0.5$ gives the best time averaged flow field prediction, and varying but somewhat good instant flow field predictions. The method thus likely needs to be altered in order to provide accurate predictions in the transitional regime.

Recall Liu's base theory that the width of the mean age distribution is related to the mixing performance, and how he used the relationship to quantify the mixing time in turbulent conditions. In that sense, the base goal is simply to use the width of the mean age distribution to quantify the mixing time, but the exact way to quantify it may be different in transitional and laminar conditions which Liu and Wu did not study. Our results indicate this, since the PDF curve needs be widened with a lower $\alpha$ in order to provide accurate predictions. Note that decreasing $\alpha$ is simply one viable method alteration to increase the PDF width and thus obtain a higher mixing time. Another option could be to integrate a larger area fraction of the PDF, e.g. 99 %.

A summary of the mixing time predictions in the transitional regime using the altered MAT method and the empirical correlations is presented in Table 9.

Table 9: Mixing time predictions of the empirical correlations, MAT with time averaged field, and MAT with mean of instant flow field predictions. MAT predictions are based on the $\alpha = 0.5$ scaling.

| **Fluid** | **Tip speed** [**m/s**] | **Re** | **Grenville** $\theta_{95}$ [**s**] | **Circulation time** $\theta_{95}$ [**s**] | **MAT time avg** $\theta_{95}$ [**s**] | **MAT instant mean** $\theta_{95}$ [**s**] | **Exp.** $\theta_{95}$ [**s**] |
|---|---|---|---|---|---|---|---|
| Fluid 2 | 4 | 1410 | 14.6 | 28.1 | 21.1 | 23.6 | 19.2 |

### 4.1.3 Laminar regime simulation

One tip speed, i.e. 2 m/s, was simulated in the laminar regime using Fluid 3 (non-Newtonian high viscosity).

#### Transient simulation

One simulation was conducted in the laminar regime using a tip speed of 2 m/s and a shear thinning fluid in accordance with Table 3. Due to the laminar conditions, we simulated both using a laminar simulation model as well as the SST k-omega turbulence model to see if the results differed. A laminar model has the advantage of being less computationally expensive. The expectation was that, if the conditions were truly laminar, that the results between the simulation models would not differ to any significant extent. We found that the velocity profiles and mixing time predictions were essentially indistinguishable, thus proving the laminar conditions. However, we continued with the turbulence model if there regardless would be any turbulence somewhere in the tank, which a laminar modell would not capture.

Time averaged velocity magnitudes for the measurement points used to determine a fully developed flow field is shown in Figure 29. For this simulation, the instant velocity magnitudes tracked over time was also analyzed when determining the fully developed flow field. Plots of these velocity magnitudes for measurement points 2 and 8 are included in the figure as well. The plots suggest that the flow is fully developed after about only 2 seconds.

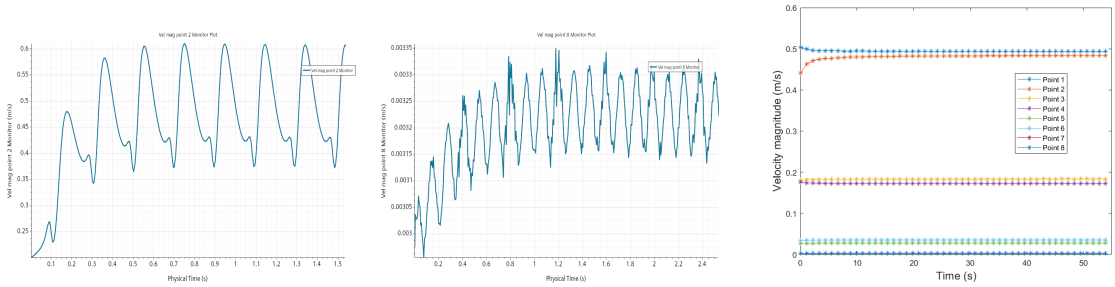


(a) (b) (c)

Figure 29: High viscosity simulation with 2 m/s TS. (a) Point 2 velocity magnitude (b) Point 8 velocity magnitude (c) Points 1-8 time averaged velocity magnitudes

The decolorization experiments in the laminar regime displayed two donut-shaped stagnant regions under each axial impeller. A picture of these regions are presented in Figure 30(c) along with the time averaged velocity magnitude profiles obtained through CFD, again at two perpendicular vertical planes.

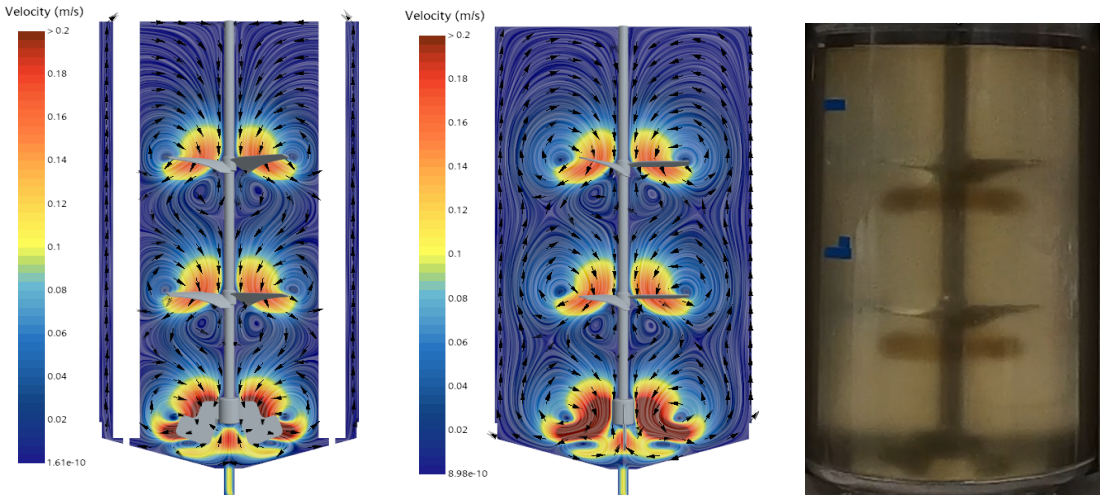


(a) (b) (c)

Figure 30: High viscosity simulation and experiment with 2 m/s TS. (a) Time averaged velocity, plane 1 (b) Time averaged velocity, plane 2 (c) Experimental trial displaying donut-shaped stagnant regions under the axial impellers

Note the recirculation zones observed under each axial impeller in the velocity profiles, which is likely an accurate prediction of the stagnant regions. This validates the prediction ability of the CFD model and demonstrates the value of using CFD in predicting mixing patterns and performance. Additionally, the velocity profiles show the slow velocities and thus slow mixing at the walls and the top of the tank, which is rather expected using this high viscosity fluid. We also see that the impellers appear to work independently of each other in comparison to the turbulent and transitional simulations. However, the tank geometry seem to aid in still obtaining a bottom to top mixing.

### Mixing time prediction using empirical methods

As described in subsection 2.4.3, the only mixing time correlation in laminar mixing was Grenville's that was based on a helical ribbon impeller, which makes it very difficult to apply to the MI setup. Regardless, an attempt was made to apply it in order to analyze it. Empirical mixing time correlations using Grenville's helical ribbon correlation and the circulation time correlation are presented in Table 10.

Table 10: Mixing time predictions using Grenville's laminar correlation for helical ribbon impellers and the circulation time correlation.

| **Fluid** | **Tip speed [m/s]** | **Re** | **Grenville $\theta_{95}$ [s]** | **Circulation time $\theta_{95}$ [s]** | **Exp. $\theta_{95}$ [s])** |
|---|---|---|---|---|---|
| Fluid3 | 2 | 115 | 240.0 | 281.0 | 1330.0 |

The empirical correlations severely underpredict the mixing time, which is relatively expected due to non of them being developed for a multi-impeller system in the laminar regime. Recall that the circulation time correlation is based on observations that about 4 circulations are required in the turbulent regime to obtain mixing. Naturally, additional circulations are expected to be required in laminar mixing, which our result agrees with. No studies were however found that that correlated the circulation time with the mixing time in the laminar regime. Despite this, one can ascertain that 19 circulations (= 392.4 s) are required, according to our CFD results, to reach complete mixing in the laminar regime for our setup.

### Mean age simulations and distributions

Recall that the impeller position at which the instant flow fields were frozen did not seem to have a meaningful impact on the mean age distribution in the turbulent and transitional simulations. In the laminar simulations, the impeller position was observed to have a slight impact on the mean age distribution. Especially, it seemed to have a larger impact than at which point in time the flow fields were frozen, why it was decided to freeze the flow fields at intervals of 60 degrees impeller rotations for a whole revolution. The flow fields of two of these impeller positions, the time averged flow field and corresponding mean age distributions are presented in Figure 31. The profiles of the original samples 1-5 are shown in Appendix B.

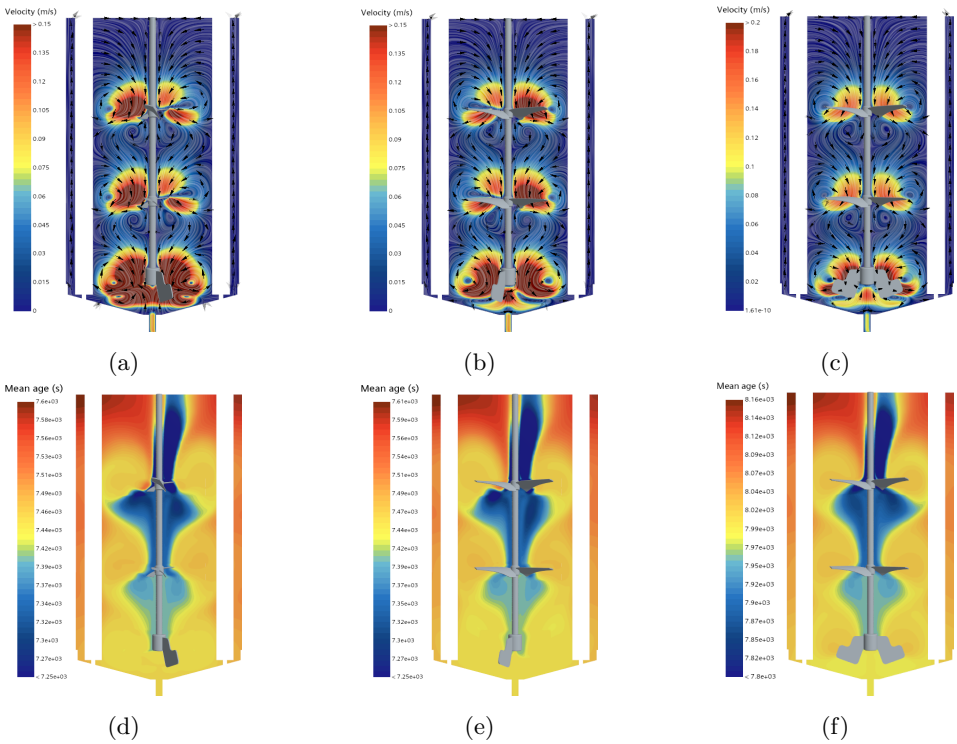


Figure 31: Velocity profiles for two instant flow fields and time averaged flow field, and corresponding mean age profiles. High viscosity simulation with 2 m/s TS. (a) & (d) Sample 1. (b) & (e) Sample 5. (c) & (f) Time averaged

Arguably quite strange is that the mean age under the axial impellers are relatively low considering the observed stagnant regions in Figure 30, which hypothetically should lead to the tracer material accumulating a high age in those regions. On the other hand, low age tracer material from the inlet also seems to be mixed down into the tank through the axial impellers, which lowers the mean age. However, if the simulated regions would truly be stagnant, then barely any tracer material should enter those regions at all. This discussion points to the difficulties that can arise when interpreting the mean age profiles. Overall, no clear conclusion can be drawn regarding the mean age of the stagnant regions. We do however see the significantly larger mean age in the top of the tank and in the corners, which points to the expected bad mixing performance in those areas.

Another important thing to consider in these laminar simulations is the turbulent and molecular Schmidt number which are used to model the mass transport of the tracer material. The turbulent Schmidt number accounts for, as the name suggests, the mass transport due to the turbulent diffusion, whereas the molecular Schmidt number account for the mass transport due to regular diffusion. In the turbulent simulations, the molecular Schmidt number appeared to have a negligible impact on the mean age simulations due to the domination of the turbulent mass transfer modeled by the turbulent Schmidt number. In the laminar simulations however, the molecular Schmidt number is the only impactful one due to the lack of turbulence. The molecular Schmidt number was, as described in subsection 3.2.2, set to 672.0 since the same was done by Wu who wrote that it was a value for sodium chloride solutions [9]. No further investigation into the Schmidt number has been made in this thesis, but might be of interest in future work for mixing time prediction in laminar conditions.

### Mean age PDF scaling and mixing time predictions

Scaled mean age PDFs for the two instant mean age fields and time averaged field presented previously is shown in Figure 32.

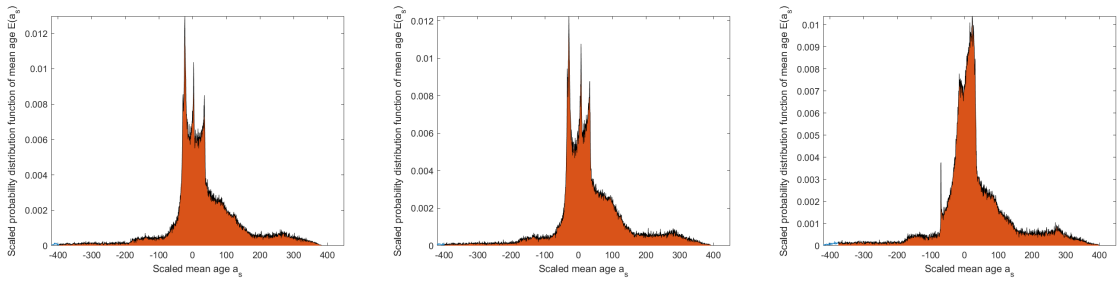


(a) (b) (c)

Figure 32: Scaled mean age PDFs using $\alpha = 0$ for two instant flow fields and the time averaged flow field. High viscosity simulation with 2 m/s TS. (a) Sample 1 (b) Sample 5 (c) Time averaged

We see that the mean age PDFs become significantly wider in these poor mixing laminar setups which agrees with the theory. However, the mixing time was severely underpredicted when integrating 95 % of the PDF area as before, leading to us having to alter the method as in the transitional regime. 99 % of the area was instead integrated scaled only using $\alpha = 0$ to obtain as wide a PDF as possible and thus as high mixing time prediction as possible. The resulting predictions using the instant and time averaged flow fields are shown in Figure 33.

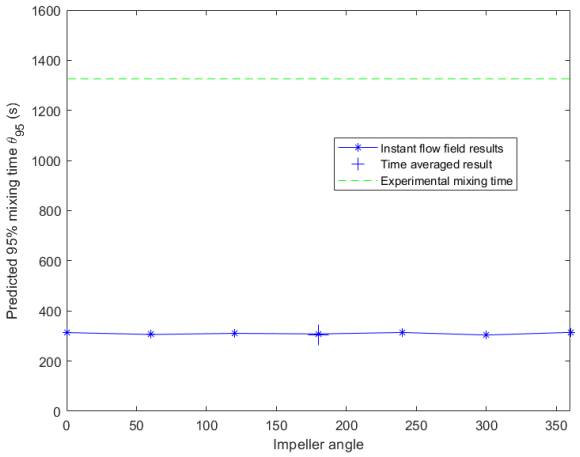


Figure 33: Mixing time predictions for seven instant flow fields at different impeller positions and the time averaged flow field, using $\alpha = 0$. High viscosity simulation with 2 m/s TS.

As is seen in the figure, CFD is unable to predict the mixing time using this MAT methodology despite altering the method. Again, MAT was developed for in turbulent conditions, and may thus not be suitable in laminar conditions in its current state. No references have been found in the literature regarding the use of MAT in laminar conditions. We do however obtain significantly wider mean age distributions, demonstrating the worse mixing performance qualitatively even though the mixing time is not accurately quantified. Additionally, as discussed before, the impact and physical relevance of the Schmidt number should be investigated in future work.

A summary of the mixing time predictions in the laminar regime using the altered MAT method and the empirical correlations is presented in Table 11.

Table 11: Mixing time predictions of the empirical correlations, MAT with time averaged field, and MAT with mean of instant flow field predictions. MAT predictions are based on the $\alpha = 0.0$ scaling.

| **Fluid** | **Tip speed** [m/s] | **Re** | **Grenville** $\theta_{95}$ [s] | **Circulation time** $\theta_{95}$ [s] | **MAT time avg** $\theta_{95}$ [s] | **MAT instant mean** $\theta_{95}$ [s] | **Exp.** $\theta_{95}$ [s] |
|---|---|---|---|---|---|---|---|
| Fluid 3 | 2 | 1410 | 240.0 | 281.0 | 304.0 | 314.0 | 1330.0 |

### 4.1.4 Mixing time prediction summary

The mixing time predictions for the MI setup using the empirical methods and the CFD methods can be summarized in a log-log plot of the dimensionless mixing time versus the Reynolds number. Again, the dimensionless mixing time is expected to be constant in the turbulent regime and decreasing with increasing Re in the transitional regime. The empirical methods and the CFD method are plotted in separate plots in Figure 34.

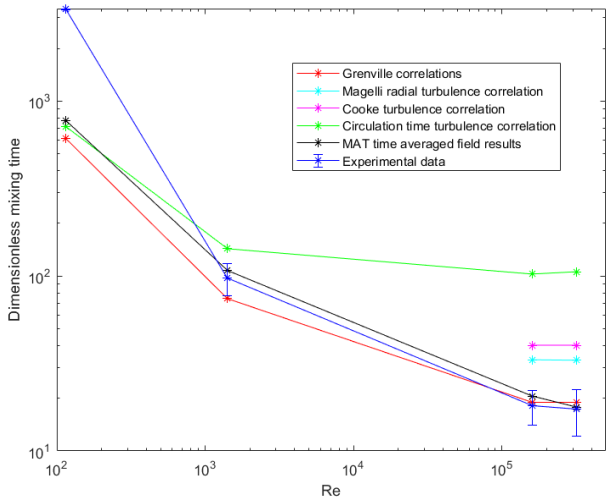


Figure 34: Dimensionless mixing time plots in log-log scale displaying predictions and experimental data for the MI setup. The bars represent +/- 2 standard deviations from the experimental data based on 2-3 experiments for each point.

The experimental mixing times are generally in agreement with the expected trend for dimensionless mixing times. Regarding the empirical methods, the plot highlights the superiority of Grenville's turbulence and transitional correlations. It also shows the overpredictions of the other correlations, especially the circulation time correlation in the turbulent regime, even though it appears to perform significantly in the laminar case. As discussed before, the circulation time correlation may be more valuable in the laminar and transitional regimes if more work is done on the amount of required circulation for mixing to be achieved. Concerning MAT, we see that the developed method using the time averaged flow field provides accurate predictions in the turbulent and transitional regime, but is not able to predict the mixing time in the laminar regime as discussed previously.

## 4.2 Single-impeller setup

Simulations were only conducted in the turbulent regime for the SI setup.

### 4.2.1 Viscojet velocity profile

Due to the Viscojet impeller not being categorized as neither a radial or axial impeller, the velocity profile at the impeller was briefly studied to understand its mixing mechanism. Velocity profiles of two perpendicular planes going through the impeller blades are shown in Figure 35.

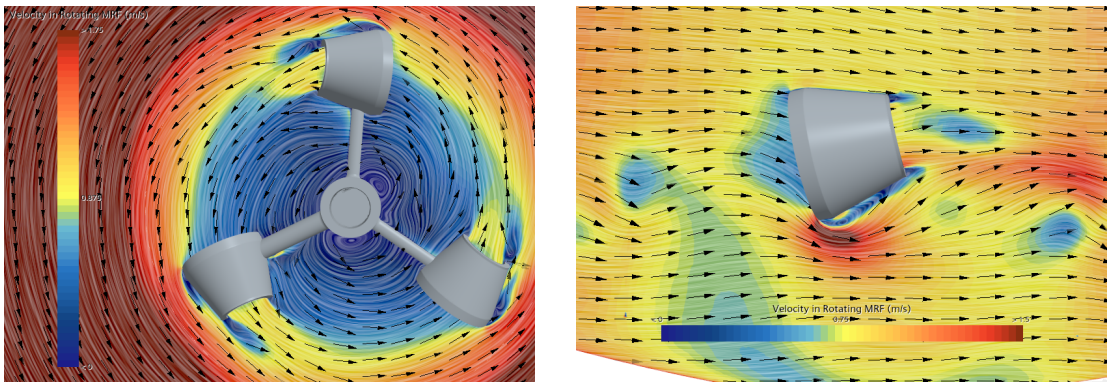


(a) (b)

Figure 35: Viscojet velocity profile (a) Horizontal plane (b) Vertical plane

We see how the velocity increases slightly when the liquid is pushed through the smaller hole as expected, but no jet is created. There is thus no strong mixing effect using these cone shaped blades.

The mixing thus appears to work seemingly satisfactory, but no exceptionally strong mixing effect is observed using these cone shaped blades.

### 4.2.2 Turbulent regime simulations

Two tip speeds, i.e. 1.8 m/s and 0.6 m/s, were simulated in the turbulent regime using Fluid 1.

#### Transient simulations

Velocity magnitudes throughout the transient simulations for measurement point 4 and 8 are depicted in Figure 36.

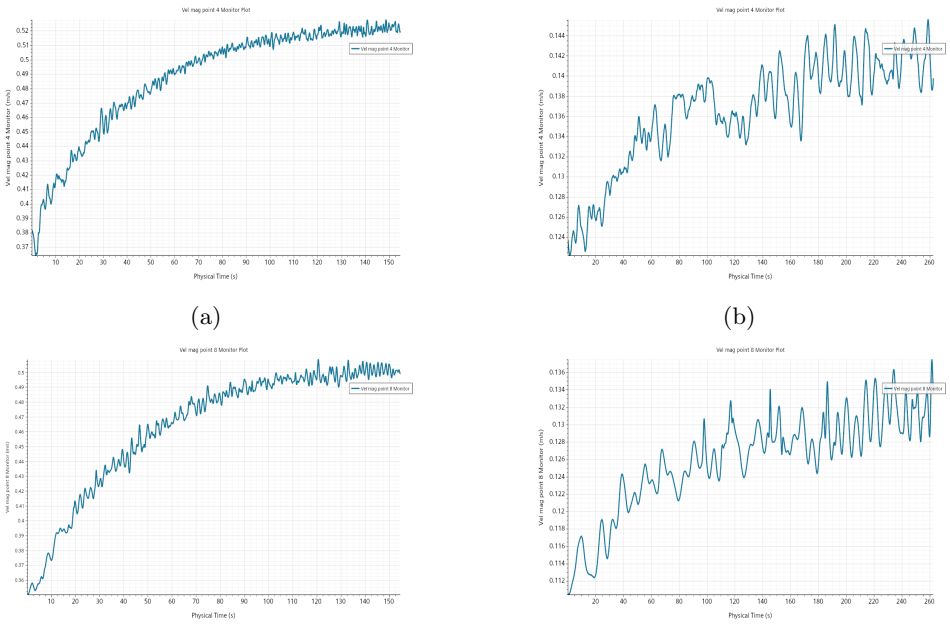

(a) (b)

(c) (d)

Figure 36: Velocity magnitude plots for two measurement points for both turbulent simulations. Low viscosity simulations. (a) Point 4, 1.8 m/s TS (b) Point 4, 0.6 m/s TS (c) Point 8, 1.8 m/s TS (d) Point 8, 0.6 m/s TS

As is seen in the figure, the flow appears to be developed after 150 s for the 1.8 m/s TS and after 250 s for the 0.6 m/s TS, which is a significantly longer time than for the MI setup. This suggests that the SI setup mixes the upper parts of the tank (e.g. point 8) much more slowly, and likely lacks a satisfactory top to bottom flow. Observing the time averaged flow fields in Figure 37 confirms this. As was done previously, (a) and (b) display the velocity along the plane for both tip speeds, whereas (c) shows the velocity magnitude profile and its direction for the 1.8 m/s TS.

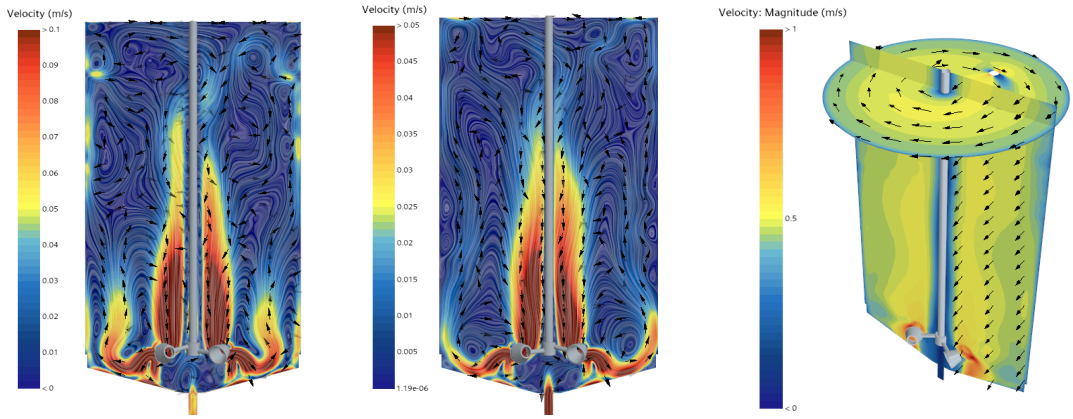


(a) (b) (c)

Figure 37: Time averaged velocity profiles. Low viscosity simulation with 1.8 m/s TS (a) Velocity profile, plane 1 (b) Velocity profile, plane 2 (c) Velocity magnitude profile, plane 1 and horizontal plane

Note that the velocities in (a) and (b) are significantly lower than the velocity magntiude, which is observed by comparing (a) and corresponding velocity magnitude in (c). The low velocity along the vertical planes highlights how the SI setup lacks the capacity to complete a continuous and circulatory flow pattern in the top half of the tank to produce a top to bottom flow. We rather see that the flow to some extent diverges inwards roughly halfway up in the tank, and then returns to the impeller along the centre of the tank, partially completing a circulation in the bottom part of the tank. In (c), we also see how the impeller mostly works to rotate the liquid, especially when considering the direction of the velocity magnitude vectors in the vertical plane. This is likely mostly due to the positioning of the impeller close to the bottom, and the lack of baffles as explained in subsection 2.1.2.

### Mixing time prediction using empirical methods

Due to the SI setup being an unbaffled single impeller system, the Magelli and Cooke correlations were deemed to not be applicable. Grenville's turbulence correlation was developed in a baffled system, but was still analyzed in this unbaffled SI setup, as was the circulation time correlation. Generally, the Karcz correlation was the only correlation found for unbaffled systems. It was also developed using varying degrees of impeller eccentricity, but a centric impeller was also included in the correlated interval [21] which was deemed to may improve the applicability of the centric SI setup. Mixing time predictions for both turbulent simulations using these empirical methods are shown in Table 12.

Table 12: Mixing time predictions using empirical correlations developed in the turbulent regime.

| **Fluid** | **Tip speed [m/s]** | **Re** | **Grenville $\theta_{95}$ [s]** | **Karcz $\theta_{95}$ [s]** | **Circulation time $\theta_{95}$ [s]** | **Exp. $\theta_{95}$ [s]** |
|---|---|---|---|---|---|---|
| Fluid 1 | 1.8 | 109000 | 25.7 | 72.2 | 142.0 | 34.2 |
| Fluid 1 | 0.6 | 36300 | 73.7 | 103.5 | 373.0 | 233.0 |

When comparing to the MI setup, the empirical predictions generally perform significantly worse. There is also no clarity in which correlation has the best prediction ability when looking at both tip speeds. Overall, the closest percentual prediction is by Grenville's correlation for the 1.8 m/s TS, but it has on the other

hand has the worst prediction for the 0.6 m/s TS. Karcz' correlation also generally performs surprisingly dissatisfactory considering it is the only correlation based on unbaffled tanks. The high aspect ratio and low impeller position of the SI setup, and generally inadequate mixing performance and lack of bottom to top flow, may be explanations for this. Karcz' correlation was developed using aspect ratios equal to 1 and a higher impeller position, as was Grenville's correlation.

### Mean age simulations and distributions

Five instant flow fields were sampled with three impeller rotations in between, as in the turbulent and transitional simulations with the MI setup. Two instant flow fields and the time averaged flow field for the 1.8 m/s TS along with their mean age distributions are shown in Figure 38. All sample profiles and scaled mean age PDFs for both the 1.8 m/s TS and 0.6 m/s TS simulations are found in Appendix B.

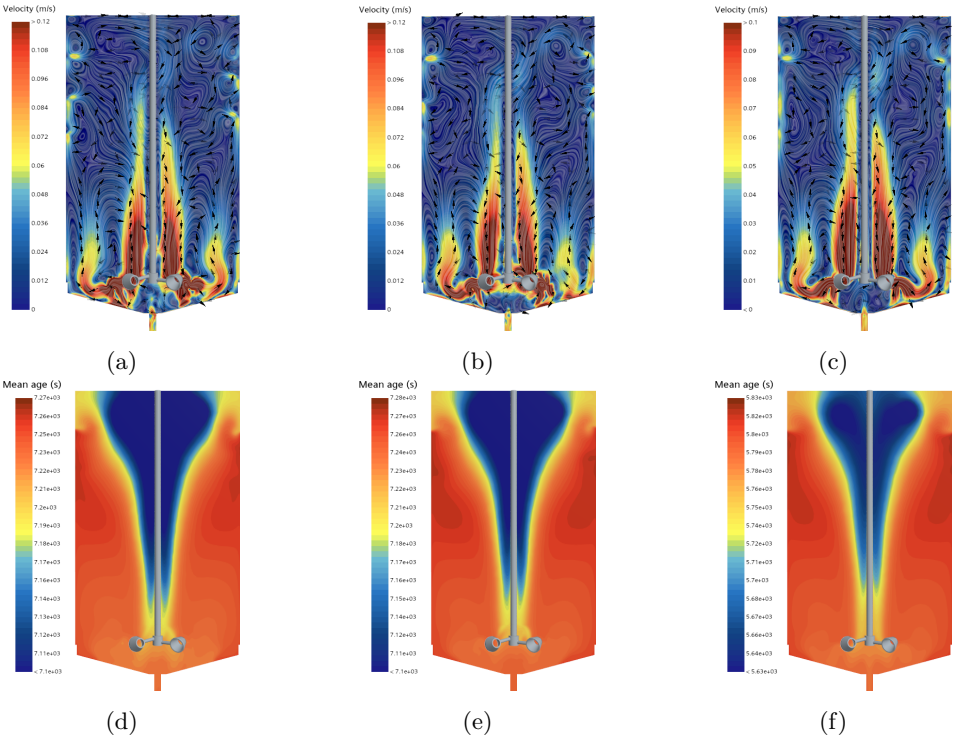


Figure 38: Velocity profiles for two instant flow fields and time averaged flow field, and corresponding mean age profiles. Low viscosity simulation with 4 m/s TS. (a) & (d) Sample 1. (b) & (e) Sample 5. (c) & (f) Time averaged

Interestingly, the mean age distributions look surprisingly similar, in comparison to the MI setup where large differences were observed. Regarding the "conical" shape of the low mean age parts, this can likely be understood by studying the velocity magnitude plots at the top of the tank. Tracer material enters through the inlet, and circulates the top parts of the tank while relatively slow being mixed down into the tank. This likely explains the low age of the tracer material in these parts. When it reaches the impeller and is pumped radially towards the walls, it has accumulated a higher age, thus explaining the higher mean age at the lower parts of the tank and at the walls. This should likely entail that mixing occurs the slowest at the walls when a tracer material is mixed into the tank.

### Mean age PDF scaling and mixing time predictions

As for the MI setup, 95 % of the scaled mean age PDF area was integrated using the four $\alpha$-values to predict the mixing times. The results for both tip speeds are depicted in Figure 39.

For the 1.8 m/s TS, the time averaged flow field using $\alpha = 2.0$ gives the closest prediction, and for 0.6 m/s TS using $\alpha = 0.5$. It is arguably quite unexpected that the original scaling gives good predictions with one tip speed but severely underpredicts at the lower tip speed. Regardless, it indicates that the MAT method requires

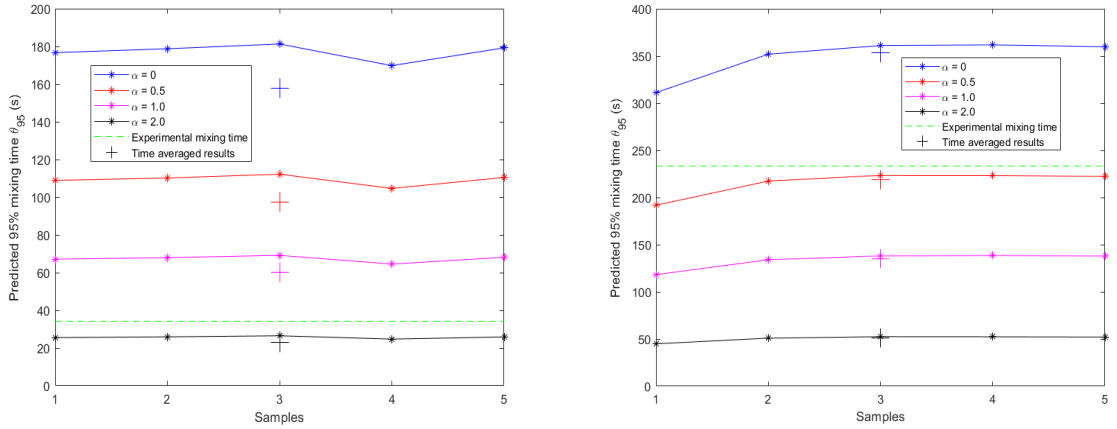


(a) (b)

Figure 39: Mixing time predictions for five instant flow field samples and time averaged flow field, using four different mean age scalings and 95 % PDF area integration. Low viscosity simulations. (a) 1.8 m/s TS (b) 0.6 m/s TS

alterations to produce accurate predictions with the SI setup. Making these alterations is generally undesired since it makes the methodology less general. In the MI setup, alterations had to be made only when moving outside the turbulent flow regime, whereas the SI setup appears to require alterations within the turbulent flow regime as is seen here. It creates difficulty in drawing more general conclusions.

A summary of the mixing time predictions in the turbulent regime using MAT and the empirical correlations is presented in Table 13.

Table 13: Mixing time predictions of the empirical correlations, MAT with time averaged field, and MAT with mean of instant flow field predictions. MAT predictions are based on the $\alpha = 0.0$ scaling.

| **Fluid** | **Tip speed [m/s]** | **Re** | **Grenville $\theta_{95}$ [s]** | **Karcz $\theta_{95}$ [s]** | **Circulation time $\theta_{95}$ [s]** | **MAT time avg $\theta_{95}$ [s]** | **MAT instant mean $\theta_{95}$ [s]** | **Exp. $\theta_{95}$ [s]** |
|---|---|---|---|---|---|---|---|---|
| Fluid 1 | 1.8 | 109000 | 25.7 | 72.2 | 142.0 | 22.9 | 25.7 | 34.2 |
| Fluid 1 | 0.6 | 36300 | 73.7 | 104.0 | 373.0 | 219.0 | 216.0 | 233.0 |

### 4.2.3 Mixing time prediction summary

The mixing time predictions for the SI setup are summarized in the dimensionless mixing time plots in Figure 40

First off, the variety of the turbulent experimental data is quite unexpected with regards to the theory, as it is expected to be constant. This may partly explain the worse performance of Grenville's correlation for the low tip speed as seen in Figure 40, since the correlation is based on a constant dimensionless mixing time with no dependence on the Reynolds number. It may however also be that the SI setup cannot be expected to have a constant dimensionless mixing time, just like the experimental data suggests. The quite odd impeller profile and bad mixing performance of the SI setup is likely quite different from setups studied by other authors. The MI setup for example has the more traditional top to bottom flow profile where the expected constant dimensionless mixing times were found experimentally. Further analysis of the SI setup with regards to these perspectives can be appropriate in future work. No general conclusion can be drawn regarding appropriate empirical correlations for the SI setup, except that Grenville's appears to give somewhat good predictions in higher tip speeds.

When observing the MAT results, the lower $\alpha$-value (and thus higher prediction) is likely required to predict the 0.6 m/s TS mixing time since its experimental value is unproportionally large considering the previously

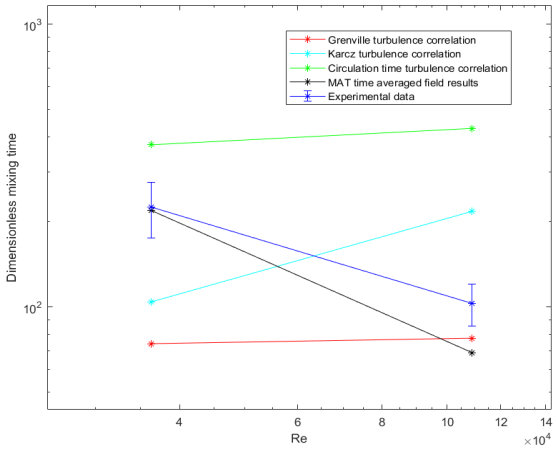


Figure 40: Dimensionless mixing time plots in log-log scale displaying predictions and experimental data for the SI setup. The bars represent +/- 2 standard deviations from the experimental data based on 2-3 experiments for each point.

discussed expectation of equally large dimensionless mixing time in turbulence.

Generally we see that the analysis becomes more complicated in the SI setup with the more odd impeller profile and worse mixing performance compared to the MI setup. The MI setup got satisfactory predictions using the same method in the turbulent regime, and required alterations only in the transitional and laminar regime, while the turbulent simulations in the SI setup required completely different scalings to obtain good predictions. Important to consider however is that Grenville's correlation gave seemingly good predictions in the MI setup, arguably lowering the need for CFD methods in mixing time prediction. The SI setup has less resemblance to traditional mixing setups, making the empirical correlations less applicable which we saw previously. A proper CFD method is thus more valuable for the SI setup.

# 5 Conclusion and future work

## 5.1 Conclusion

In this thesis, the use of empirical mixing time correlations was successfully analyzed in a 200 L high aspect ratio tank with two different agitators; one multi-impeller setup with baffles (MI setup) and one single impeller setup without baffles (SI setup). A mixing time prediction method based on CFD and MAT was also developed and analyzed for both setups.

### 5.1.1 Multi-impeller setup

- Grenville's [19] turbulent and transitional mixing time correlations perform well for the MI setup, and likely perform similarly in other comparable high aspect multi-impeller setups with a satisfactory mixing performance. Other turbulent correlations function significantly worse for the MI setup, but are likely to make better predictions in setups with conditions more similar to those under which these correlations were developed, such as using multiple identical impellers as in the Magelli [20] correlation or multiple Rushton turbines as in the Cooke [15] correlation.
- Regarding the CFD method, we found that applying original MAT author Liu's [8] approach while using time averaged flow fields with a SM method provides accurate mixing time predictions for the MI setup in the turbulent regime, suggesting the method is usable in similar setups. In the transitional regime, the method has to be tweaked by lowering the $\alpha$-value (Equation 40) from 2.0 to 0.5 to give accurate predictions. Regardless, using the CFD method is much less valuable in the turbulent and transitional regime where Grenville's more practical correlation makes such accurate predictions.
- In the laminar regime, the empirical correlations used lacked applicability on the MI setup and were thus not able to predict the mixing time. The CFD method based on MAT could not predict the mixing time as well even after several tweaks, which is partly because the method has previously not been studied in the transitional and laminar regimes. However, improving the MAT method to give better predictions or using other CFD methods is highly valuable in the laminar regime where there is a lack of reliable empirical correlations.

### 5.1.2 Single-impeller setup

- All studied empirical correlations provided dissatisfactory predictions for the SI setup, which is highly likely due to its quite odd impeller profile, inadequate mixing performance and lack of bottom to top flow. The correlations were developed using more standard tank setups, and may thus perform better in other unbaffled single-impeller setups. Especially the Karcz [21] correlation which was the only correlation developed using unbaffled tanks found in this thesis.
- Regarding the CFD method, applying Liu's approach using a SM method appears to give relatively good predictions at higher impeller speeds. At the lower impeller speed, changing $\alpha$ from 2.0 to 0.5 was required to predict the mixing time. Generally, these method alterations reduces the method's robustness and makes it more reliable on experimental data in order to know how the method should be tweaked.
- Similar to the argument made in the laminar regime, improving the CFD method or using other CFD methods can be very valuable in these more odd tank setups where empirical correlations perform worse.

## 5.2 Future work

Based on our results, it is recommended to use Grenville's [19] turbulent and transitional correlations in the MI setup or similar setups for accurate mixing time predictions. Using CFD with MAT is not valuable in these scenarios due to the practicality of the correlations and the method tweaking required with MAT in the transitional regime.

CFD remains more useful when mixing time correlations are less applicable and perform worse, for example in the laminar regime and for more odd setups like the SI setup. However, in these scenarios, the MAT method in its current state is not the ideal CFD method to use due to the tweaking required which makes it more reliable on experimental data. It is thus recommended to utilize more robust CFD methods for mixing time predictions in these setups.

MAT should not be disregarded altogether. It still provides accurate predictions in the turbulent regime for the higher performing MI setup, and both Liu [8] and Wu [9] found it very useful. Future studies of the method outside the standard turbulent setups may make it a viable and valued CFD alternative. Additionally, a remark should be made regarding Liu's and Wu's use of a MRF flow field with MAT compared to our use of a SM. Even though this thesis has discussed the significant disadvantages of using MRF in rotationally assymetric tank setups, it is approximately twenty times less computationally expensive than the SM method, as highlighted by Liu and Wu [8, 9]. Studying the viability of a MRF method with MAT may thus still be of interest in future work as well.

The other mixing time correlations analyzed in this thesis should be studied in other more relevant setups where they can be more valuable. Especially the Karcz [21] correlation can potentially be very useful in more standard unbaffled setups, since it was the only unbaffled correlation found in this thesis.

# References


[1] E. Nauman. *Residence Time Distributions*, pages 1–17. Wiley Online Books, 2004.

[2] R. R. Hemrajani and G. B. Tatterson. *Mechanically Stirred Vessels*, pages 345–390. Wiley Online Books, 2004.

[3] M. F. Edwards, M. R. Baker, and J. C. Godfrey. Chapter 8 - mixing of liquids in stirred tanks. *Mixing in the Process Industries*, pages 137–158, 1997.

[4] A. K. Coker. *Modeling of chemical kinetics and reactor design.* Gulf Professional, 2. edition, 2001.

[5] D. E. Leng and R. V. Calabrese. *Immiscible Liquid-Liquid Systems*, pages 639–753. Wiley Online Books, 2004.

[6] V. A. Penney, W. R. andAtiemo-Obeng. *Heat Transfer*, pages 869–886. Wiley Online Books, 2004.

[7] E. M. Marshall and A. Bakker. *Computational Fluid Mixing*, pages 257–343. Wiley Online Books, 2004.

[8] G. Ascanio. Mixing time in stirred vessels: A review of experimental techniques. *Chinese Journal of Chemical Engineering*, 23(7):1065–1076, 2015.

[9] M. Wu, N. Jurtz, A. Walle, and M. Kraume. Evaluation and application of efficient cfd-based methods for the multi-objective optimization of stirred tanks. *Chemical Engineering Science*, 263, 2022.

[10] *Frontmatter*, pages i–lxi. Wiley Online Books, 2004.

[11] Visco Jet. Tank agitator for installation from above. https://viscojet.de/en/portfolio/tank-agitators-visco-jet-vj500/. Accessed: 2024-05-01.

[12] S. M. Kresta and R. S. Brodkey. *Turbulence in Mixing Applications*, pages 19–87. Wiley Online Books, 2004.

[13] Ghotli R. A., Raman A. A. A., S. Ibrahim, and S. Baroutian. Liquid-liquid mixing in stirred vessels: A review. *Chemical Engineering Communications*, 200(5):595–627, 2013.

[14] A. Paar. Basics of rheology. https://wiki.anton-paar.com/en/basics-of-rheology/. Accessed: 2024-05-08.

[15] R. K. Grenville and A. W. Nienow. *Blending of Miscible Liquids*, pages 507–542. Wiley Online Books, 2004. Wiley Online Books.

[16] D. A. R. Brown, P. N. Jones, J. C. Middleton, G. Papadopoulos, and E. B. Arik. *Experimental Methods*, pages 145–256. Wiley Online Books, 2004.

[17] A. B. Metzner and R. E. Otto. Agitation of non-newtonian fluids. *AIChE Journal*, 3(1):3–10, 1957.

[18] G. Ascanio. Mixing time in stirred vessels: A review of experimental techniques. *Chinese Journal of Chemical Engineering*, 23(7):1065–1076, 2015.

[19] R. K. Grenville. *Blending of viscous Newtonian and pseudo-plastic fluids.* Electronic thesis or dissertation, Cranfield Institute of Technology, 1992.

[20] F. Magelli, G. Montante, D. Pinelli, and A. Paglianti. Mixing time in high aspect ratio vessels stirred with multiple impellers. *Chemical Engineering Science*, 101:712–720, 2013.

[21] J. Karcz, M. Cudak, and J. Szoplik. Stirring of a liquid in a stirred tank with an eccentrically located impeller. *Chemical Engineering Science*, 60(8-9):2369–2380, 2005.

[22] Y. Sano and H. Usui. Interrelations among mixing time, power number and discharge flow rate number in baffled mixing vessels. *Journal of Chemical Engineering of Japan*, 18(1):47–52–52, 1985.

[23] P. M. Doran. *Bioprocess engineering principles.* Academic, second edition. edition, 1995.

[24] F. R. Menter. Two-equation eddy-viscosity turbulence models for engineering applications. *AIAA Journal*, 32(8):1598–1605, 1994.

[25] Siemens Digital Industries Software. Simcenter STAR-CCM+, version 2310, Siemens 2023.

[26] MultiMedia LLC. Sst k-omega model. http://web.archive.org/web/20080207010024/http://-www.808multimedia.com/winnt/kernel.htm, 1999. Accessed: 2024-04-15.

[27] M. Liu. *Mean Age Theory for Quantitative Mixing Analysis.* John Wiley & Sons, 2015, 2015. Wiley Online Books.

[28] O. Lundstrom and H. Syrjä. Study of particle homogeneity in mixing tanks using experiments and cfd [master's thesis, lund university], 2021. https://lup.lub.lu.se/student-papers/search/publication/9040956.

[29] S. Poveda Ruiz. Study of flow fields in mixing tanks with particles using cfd [master's thesis, lund university], 2021. https://lup.lub.lu.se/student-papers/search/publication/9061383.

[30] T.L. Rodgers, L. Gangolf, C. Vannier, M. Parriaud, and M. Cooke. Mixing times for process vessels with aspect ratios greater than one. *Chemical Engineering Science*, 66(13):2935–2944, 2011.

[31] M. Wu, N. Jurtz, L. Hohl, and M. Kraume. Multi-impeller mixing performance prediction in stirred tanks using mean age theory approach. *AIChE Journal*, 70(1), 2024.

# Appendices

## A Obtaining time averaged flow fields

Time averaged flow fields are obtained by averaging all solved flow variables, e.g. velocity, pressure and turbulence variables, over time. In this thesis, samplings of all variables were made at every time step during the transient simulation. Ideally, sampling were to be started after the flow field was fully developed in order to minimize the effect of the initial transient on the time averaged field. This was not realized until the later parts of the thesis work, which led to the sampling starting three seconds into the transient simulation for the MI setup, before it was known whether or not the flow was fully developed. The time averaging was redone for the low viscosity 2 m/s simulation by starting the time averaging later, whereas the remaining MI setup were not redone. For the SI setup however, the sampling started after the flow field was developed for all simulations.

Obtaining the time averaged flow fields in the stationary region of the tank was quite simple using the software's built in function for time averaging. It was however more complicated in the rotating regions since the mesh itself is rotating with the impeller blades. The built in time averaging function in STAR CCM+ works by averaging the field variables in each cell, which entails that it is the same cells that always are in the area with high velocity behind the impeller blades, and the same cells that are further away in the low velocity parts of the rotating regions. This was problematic since the desire was to time average at static points in space in the rotating regions rather than in the rotating cells.

This was dealt with using a methodology where the flow variables in the rotating regions were, at each time step, mapped to identical but stationary regions that lacked the moving impeller blades. These regions are referred to as "dummy regions". The variables were to be mapped to all parts of the stationary dummy regions except for the position of the impeller blades, since that would give an unrealistic contribution to the time averaging. The dummy regions contained only the essential physics settings to enable them to be meshed, see Table 14. The rotating regions for the MI and SI setups and their corresponding dummy regions are displayed in Figure 41.

Table 14: Physics for dummy regions

| **Setting** | **Chosen option/value** |
|---|---|
| 3D | Activated |
| Implicit unsteady | Activated |
| Solution Interpolation | Activated |

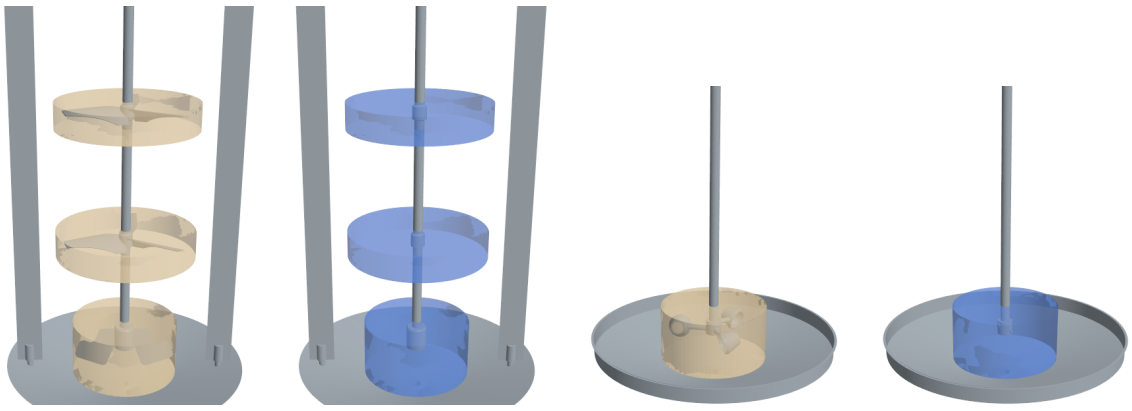

(a) (b) (c) (d)

Figure 41: (a) MI setup rotating regions (b) MI setup dummy regions (c) SI setup rotating region (d) SI setup dummy region

The time averaging was achieved using a series of connected field functions, the first of which had the purpose of keeping track of the position of the impeller blades. This user defined field function, "Outside_Impeller", is presented in Equation 42 with STAR CCM+ syntax. The field function assumes a value of 1 in all non impeller positions and a value of 0 in the impeller positions. The geometry part "Impeller Blades" consisted only of the moving parts of the impellers, i.e. the blades.

$$\text{Outside\_Impeller} = 1 - \text{insidePart}(\text{@GeometryPart}(\text{"Impeller Blades"})) \tag{42}$$

All mapped field variables were described by their own field function that were updated every time the variables are mapped, i.e. at every time step. Here, the general form of these field functions are referred to as "Mapped_Variable". The field functions were filtered by multiplication with "Outside_Impeller" to prevent mapping of the values at the position of the impeller blades, which was done by creating new filtered field functions for all mapped variables. See Equation 43.

$$\text{Filtered\_Variable} = \text{Mapped\_Variable} \times \text{Outside\_Impeller} \tag{43}$$

For this filtering to work properly and filter at the current position of the impeller blades, a rotating motion transformation corresponding to the impeller speed was applied to the geometry part "Impeller Blades". Additionally, the remesher setting was activated with the impeller transformation as input. This was essential for the filtered mapping to work properly.

After setting up the variable filtering, field functions monitoring the sum of all filtered mapped variables to the dummy regions were set up, as well as a field sum monitor tracking the total number of samples at each position in the mapped stationary region. These field functions are referred to as "Filtered_Variable_Sum" and "Sample_Sum", respectively. These field functions were used to calculate the mean of the mapped field variables, which was done through new field functions defined as in Equation 44.

$$\text{Filtered\_Mean\_Variable} = \text{Filtered\_Variable\_Sum}/\text{Sample\_Sum} \tag{44}$$

Through these connected field functions, a time averaged flow field was obtained in the rotating regions throughout the transient simulations. The transient simulations continued until the flow field was considered to be fully developed.

# B Velocity profiles, mean age profiles and scaled PDFs

## B.1 MI setup

### B.1.1 Turbulence

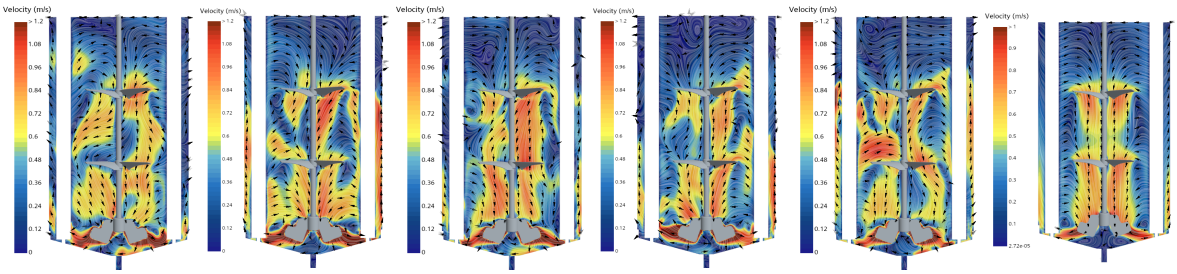


(a) (b) (c) (d) (e) (f)

Figure 42: Velocity profiles 4 m/s TS. (a)-(e) Samples 1-5. (f) Time averaged

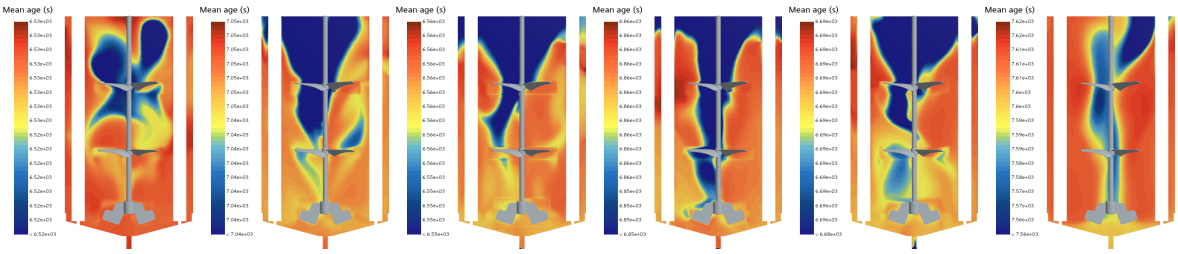


(a) (b) (c) (d) (e) (f)

Figure 43: Mean age profiles 4 m/s TS. (a)-(e) Samples 1-5. (f) Time averaged

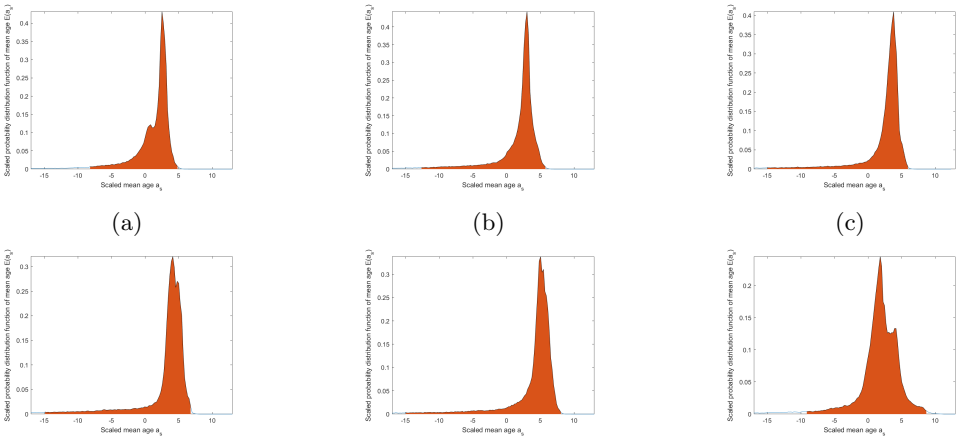

(a) (b) (c)

(d) (e) (f)

Figure 44: PDFs, $\alpha = 2.0$, 4 m/s TS. (a)-(e) Samples 1-5. (f) Time averaged

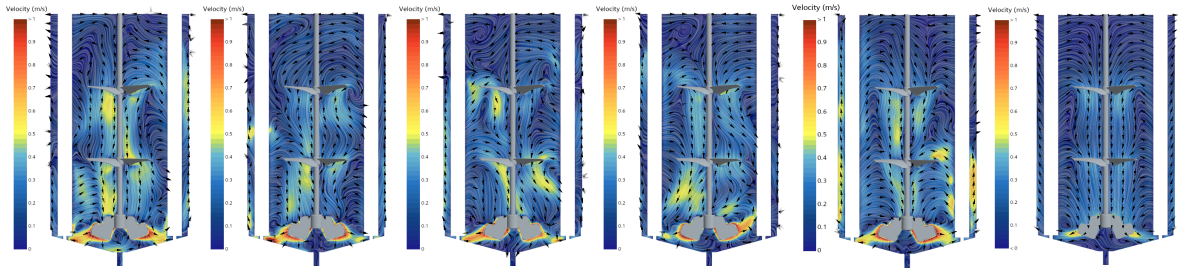

(a) (b) (c) (d) (e) (f)

Figure 45: Velocity profiles 2 m/s TS. (a)-(e) Samples 1-5. (f) Time averaged

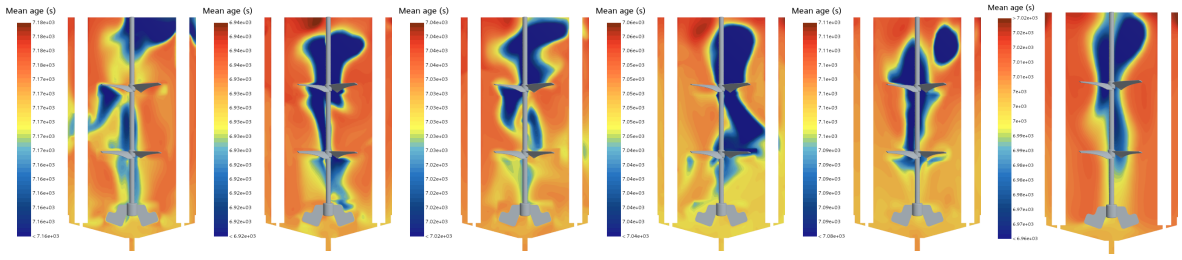

(a) (b) (c) (d) (e) (f)

Figure 46: Mean age profiles 2 m/s TS. (a)-(e) Samples 1-5. (f) Time averaged

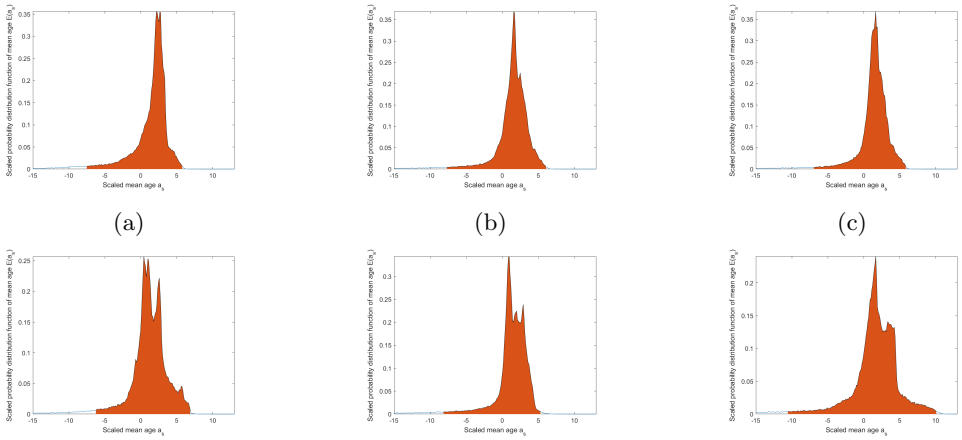

(a) (b) (c)

(d) (e) (f)

Figure 47: PDFs, $\alpha = 2.0$, 2 m/s TS. (a)-(e) Samples 1-5. (f) Time averaged

### B.1.2 Transitional

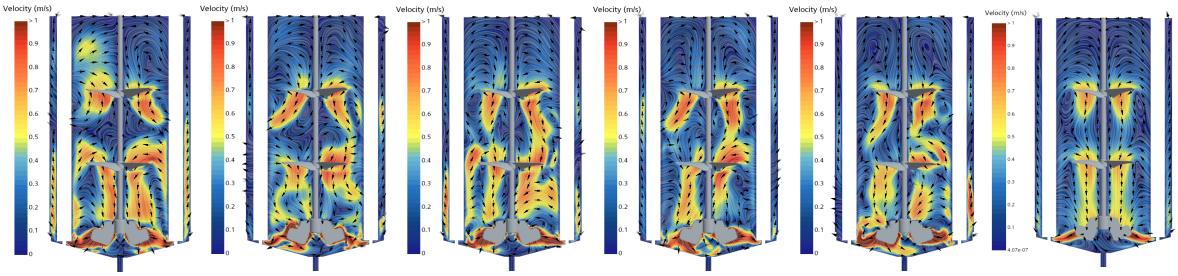

(a) (b) (c) (d) (e) (f)

Figure 48: Velocity profiles 4 m/s TS. (a)-(e) Samples 1-5. (f) Time averaged

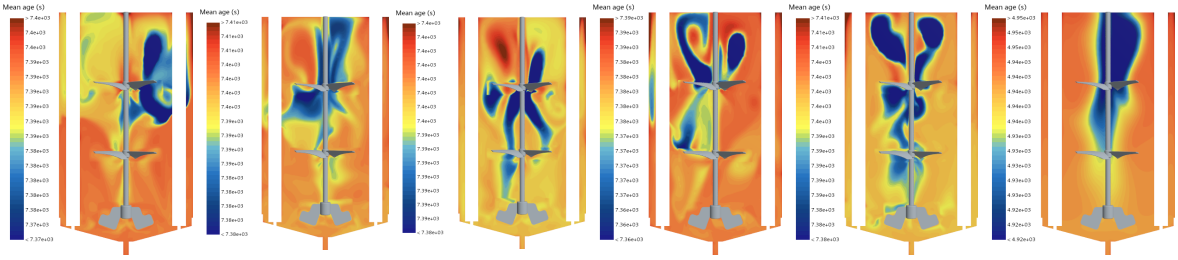

(a) (b) (c) (d) (e) (f)

Figure 49: Mean age profiles 4 m/s TS. (a)-(e) Samples 1-5. (f) Time averaged

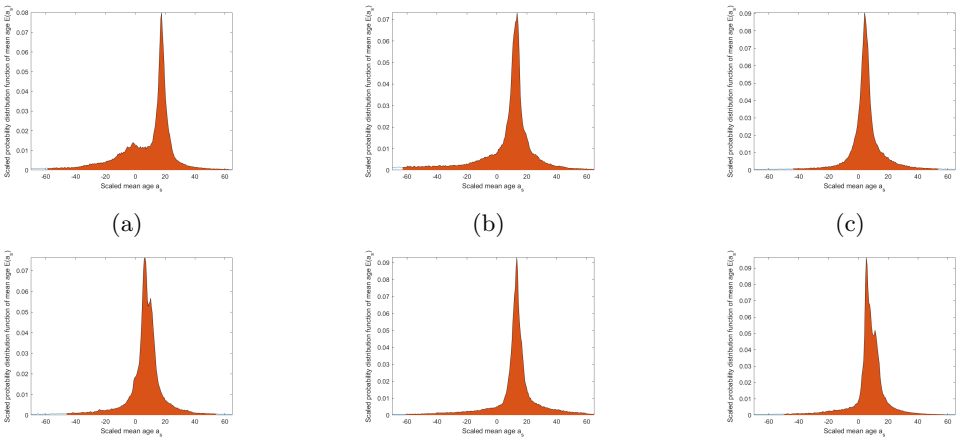

(a) (b) (c)

(d) (e) (f)

Figure 50: PDFs, $\alpha = 0.5$, 4 m/s TS. (a)-(e) Samples 1-5. (f) Time averaged

### B.1.3 Laminar

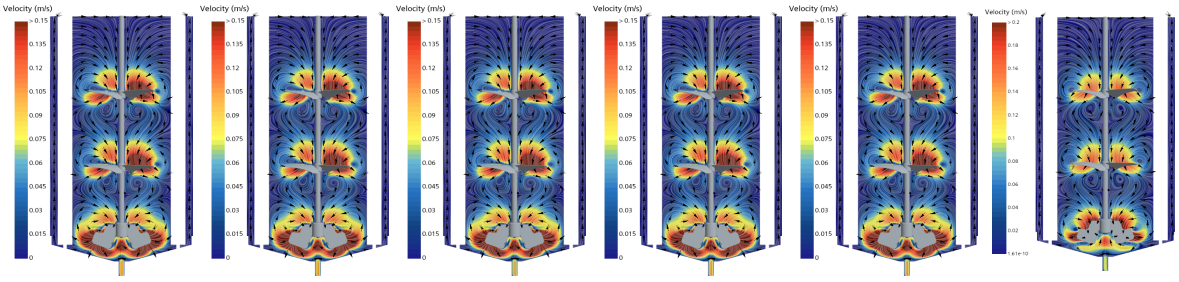

(a) (b) (c) (d) (e) (f)

Figure 51: Velocity profiles 2 m/s TS. (a)-(e) Samples 1-5. (f) Time averaged

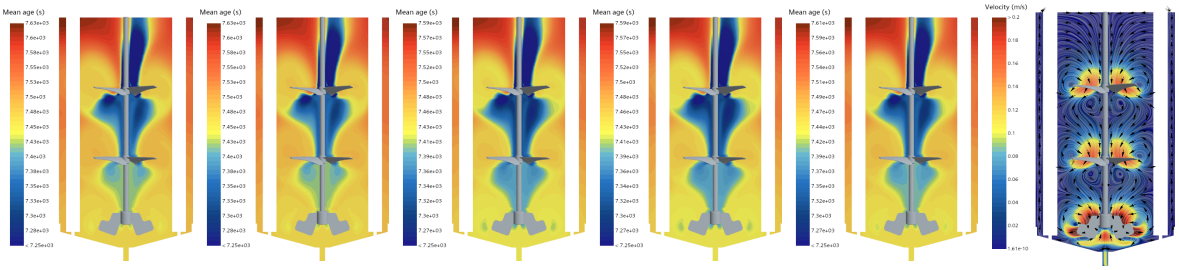

(a) (b) (c) (d) (e) (f)

Figure 52: Mean age profiles 2 m/s TS. (a)-(e) Samples 1-5. (f) Time averaged

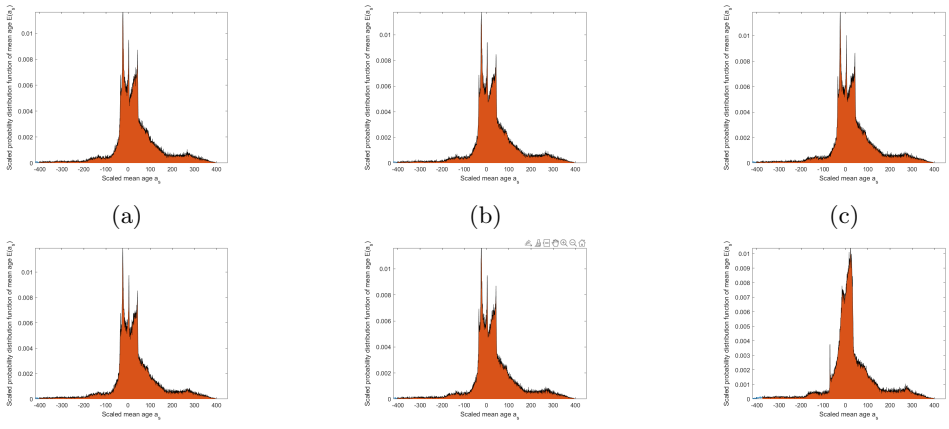

(a) (b) (c)

(d) (e) (f)

Figure 53: PDFs, $\alpha = 0.0$, 2 m/s TS. (a)-(e) Samples 1-5. (f) Time averaged

## B.2 SI setup

### B.2.1 Turbulence

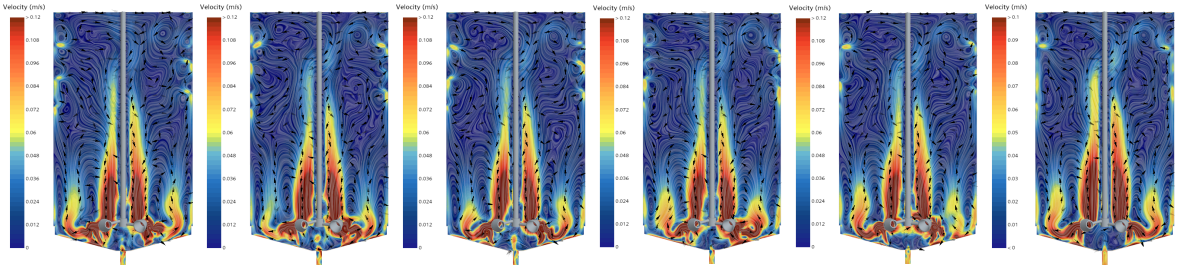

(a) (b) (c) (d) (e) (f)

Figure 54: Velocity profiles 1.8 m/s TS. (a)-(e) Samples 1-5. (f) Time averaged

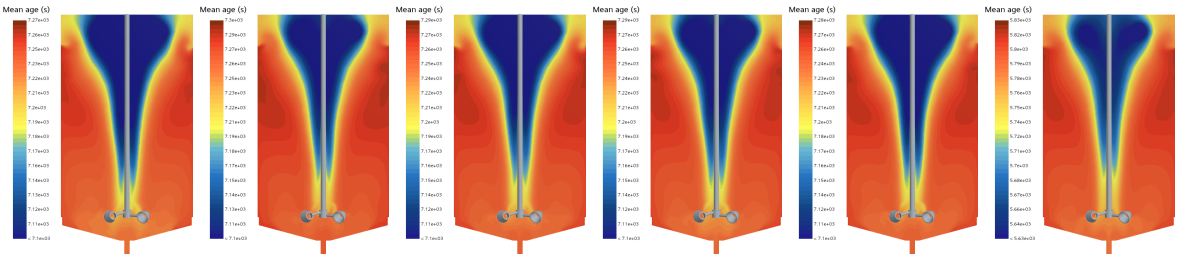

(a) (b) (c) (d) (e) (f)

Figure 55: Mean age profiles 1.8 m/s TS. (a)-(e) Samples 1-5. (f) Time averaged

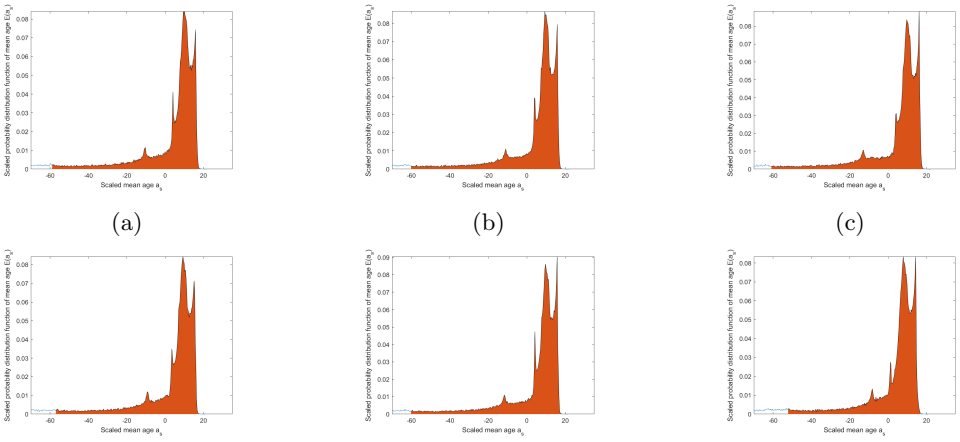

(a) (b) (c)

(d) (e) (f)

Figure 56: PDFs, $\alpha = 2.0$, 1.8 m/s TS. (a)-(e) Samples 1-5. (f) Time averaged

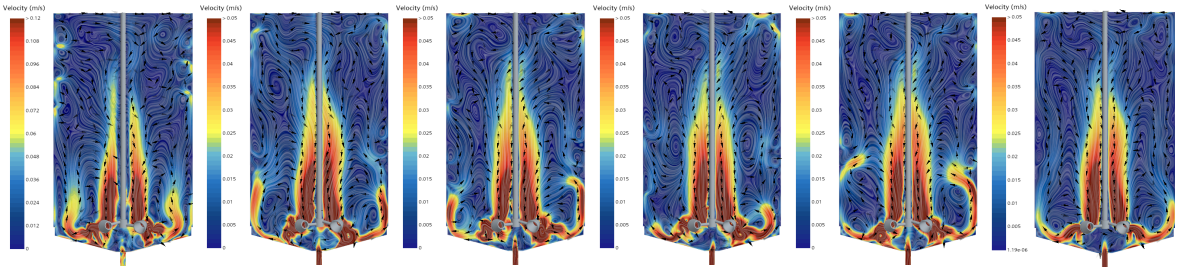

(a) (b) (c) (d) (e) (f)

Figure 57: Velocity profiles 0.6 m/s TS. (a)-(e) Samples 1-5. (f) Time averaged

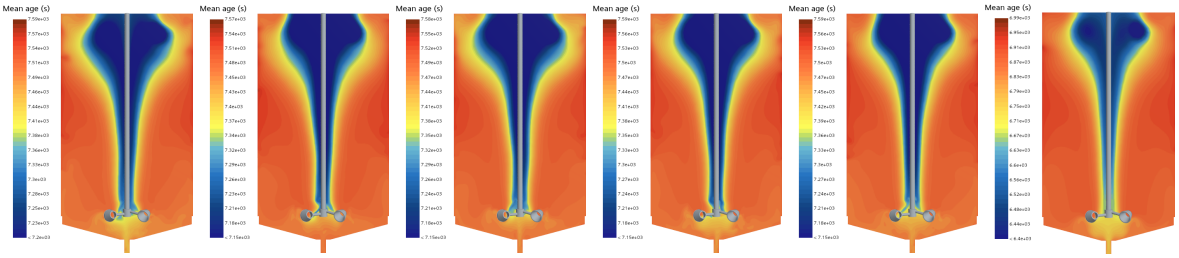

(a) (b) (c) (d) (e) (f)

Figure 58: Mean age profiles 0.6 m/s TS. (a)-(e) Samples 1-5. (f) Time averaged

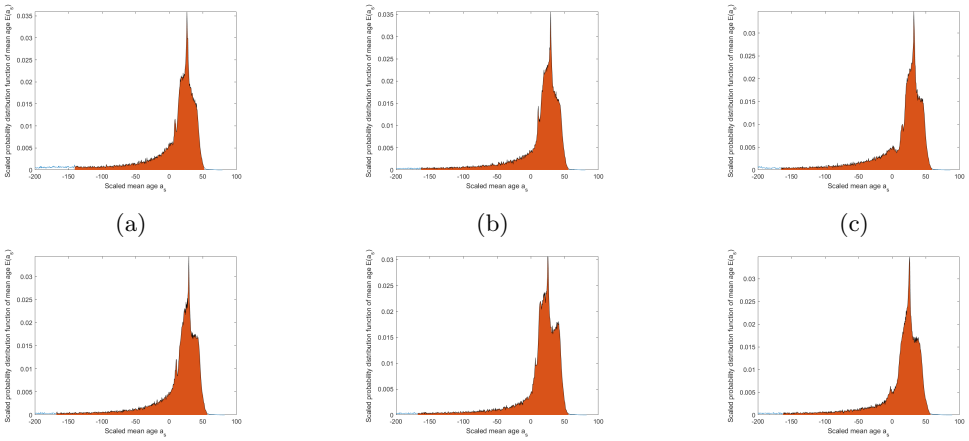

(a) (b) (c)

(d) (e) (f)

Figure 59: PDFs, $\alpha = 0.5$, 0.6 m/s TS. (a)-(e) Samples 1-5. (f) Time averaged